

THE STELLAR HALOS OF MILKY WAY
TYPE GALAXIES IN THE EAGLE
SIMULATIONS

Samuel Robert John Walton

A thesis submitted in partial fulfilment of the requirements of
Liverpool John Moores University
for the degree of
Master of Philosophy.

October 2017

Contents

List of Figures	i
Declaration	iii
Abstract	iv
1 Introduction	1
1.1 Stellar halos	2
1.2 The Milky Way	8
1.3 The Andromeda Galaxy (M31)	11
1.4 The EAGLE simulations	12
1.4.1 Subgrid physics	15
2 Stellar halos in EAGLE	18
2.1 Galaxy selection	18
2.2 Separating accreted and in situ stars	23
2.3 Density and surface brightness profiles	26
2.4 Metallicity distribution	30
2.5 Subgrid physics	37

2.6	Halo dependence on substructure	39
2.7	Outer stellar halo fractions	43
3	Conclusions	46
4	Future Work	49
4.1	Metallicity profiles	49
4.2	Stellar halo diversity	50
4.3	Stellar halo fractions	51
	Bibliography	52

List of Figures

2.1	Probability distribution of J_z/J_{circ} for one galaxy in the L0025N0752 galaxy sample	20
2.2	Edge-on density maps of the L0025N0752 galaxies before D/T cut	22
2.3	Virial radius and stellar mass distribution of the two EAGLE galaxy samples	23
2.4	Accretion fraction profiles for the L0025N0752 galaxy sample	25
2.5	Surface density profile of the L0100N1504 galaxy sample . . .	27
2.6	Surface density broken power law fit	28
2.7	Surface brightness profile for the L0100N1504 galaxy sample .	29
2.8	Metallicity distribution functions for both galaxy samples . .	31
2.9	Radial metallicity profile for both galaxy samples	32
2.10	Distribution of metallicity gradients for the L0100N1504 galaxy sample	33
2.11	Individual radial metallicity profiles for the L0025N0752 galaxy sample	34

2.12 2D metallicity map for one galaxy in the L0025N0752 galaxy sample	35
2.13 Radial metallicity profile for the L0100N1504 galaxy sample, also split into accreted and in situ components	36
2.14 Radial metallicity and density profiles for the L0050N0752 model variation galaxy samples	38
2.15 Mass-metallicity relation for $z = 0$ satellites of both galaxy samples	40
2.16 Mass-metallicity relation of galaxy satellites in the StrongFB and WeakFB runs	41
2.17 Correlation between the $z = 0$ satellite mass-metallicity rela- tion and galaxy radial metallicity gradient	42
2.18 Stellar halo mass fractions for a galaxy sample with a wider mass range	44

Declaration

The work carried out in this thesis was carried out at the Astrophysics Research Institute, Liverpool John Moores University. Unless otherwise stated, it is the original work of the author.

While registered as a candidate for the degree of Master of Philosophy, for which submission is now made, the author has not been registered as a candidate for any other award. This thesis has not been submitted in whole, or in part, for any other degree.

Sam Walton
Astrophysics Research Institute
Liverpool John Moores University
IC2, Liverpool Science Park
146 Brownlow Hill
Liverpool
L3 5RF
United Kingdom

Abstract

The stellar halo component of a galaxy contains a wealth of valuable information on the host galaxy’s formation history. As the diffuse outskirts of galaxies which have been built up through hierarchical assembly, their content and structure is directly tied to the material that was accreted onto them over the course of the galaxy’s life. This thesis presents the results of a study into the stellar halos of Milky Way (MW) type galaxies in the EAGLE simulations.

Analysis was primarily carried out on two data sets from the EAGLE simulations; one set of 352 galaxies (from the ‘Reference’ model) and 9 higher resolution galaxies (from a ‘recalibrated’ smaller box size model). Galaxies were selected with criteria of approximately the MW halo mass and a prominent disc component. We find that EAGLE is able to reproduce a number of observational properties of stellar halos, including the surface brightness and density profiles. This lends weight to the suitability of cosmological simulations to accurately model stellar halos, and in particular shows that EAGLE is a good basis for deeper analysis of MW-mass disc galaxy stellar halos.

Negative metallicity gradients are ubiquitous in the galaxy samples analysed, with gradients in the range -0.002 to -0.02 dex kpc^{-1} , consistent with recent observations of M31. The gradient was found to be primarily driven by the transition from high metallicity in situ stars to low metallicity accreted stars with increasing radius, and sensitive to the simulation feedback efficiency employed in the simulation. The in situ and accreted components individually, however, do both have negative metallicity gradients. Observations of some galaxies, including the MW, find flat metallicity profiles, with one proposed explanation being the tendency to observe along only the minor axis. Measuring along the minor or major axes in this simulated galaxy sample does not explain the lack of gradients found in observational data as we fail to reproduce any flat metallicity profiles. Altering the feedback efficiency does, however, have an effect on the metallicity gradients, with weak feedback resulting in shallower gradients.

The results are not strongly sensitive to the AGN subgrid parameters adopted in the EAGLE simulations. When tested against runs with varied stellar feedback efficiency, we find that the metallicity is affected by up to a few tenths of a dex, with the Reference model having higher metallicity out to around $40 - 50\text{kpc}$. The density profiles were not altered significantly in the regions analysed here, with only the central - bulge dominated - region differing between model runs.

No correlation was found between the mass-metallicity relation of a galaxy's $z = 0$ satellite population and its stellar metallicity gradient, and testing against two extreme EAGLE models showed that feedback strength had no effect on the gradient of the $z = 0$ mass-metallicity relation. While

strong and weak stellar feedback changed the absolute metallicity of galaxy satellites, the overall mass-metallicity gradient remained the same.

The outer stellar halo fractions of galaxies in a wider mass range were measured for comparison with recent observational stellar halo surveys and found to be generally higher, with no galaxies having an undetectable stellar halo unlike for certain galaxies recently observed. The stellar halo mass fraction of EAGLE galaxies was found to be correlated with galaxy stellar mass, with the mean fraction rising from 1% at $M_* \sim 5 \times 10^9 M_\odot$ to 18% at $M_* \sim 5 \times 10^{11} M_\odot$. The sample has an overall mean halo mass fraction of 3%, ranging from 0.1% to 30%.

Chapter 1

Introduction

Looking past the hundreds of billions of foreground stars contained within our own Galaxy, the Milky Way (MW), we find that the universe is filled with a diverse range of galaxies. From dwarf galaxies containing just tens or hundreds of millions of stars, through to giant elliptical galaxies containing trillions, we are tasked with the challenge of finding a model that can accurately describe a huge range of galaxy properties.

The currently favoured cosmological Λ -Cold Dark Matter (Λ CDM) model explains that this diversity is a result of hierarchical assembly, with galaxies building up over time through the accretion and merging of smaller galaxies. A direct consequence of this evolution is the build up of material in a diffuse and extended region around galaxies. This outer region - the stellar halo - can aid in understanding the history of a galaxy, by serving in part as an archaeological record of its merger history.

This chapter summarises the relevant work carried out so far to understand galaxies' stellar halos in an effort to gain broader understanding of

galaxy formation and evolution.

1.1 Stellar halos

Surrounding the majority of the stars in our Galaxy, which reside in the disc and bulge components, an extended and diffuse stellar halo contains the oldest and most metal-poor stars yet observed (Helmi, 2008). Beyond the MW, stellar halos are now being observed in a range of galaxies of varying distances, sizes, and types; the best observed of these being our neighbour M31 (e.g. Ibata et al., 2014), with surveys such as GHOSTS (Radburn-Smith et al., 2011) looking at other galaxies in the local volume ($\lesssim 20$ Mpc), or investigating stellar populations in the outskirts of more distant galaxies up to $z \sim 1$ (Trujillo and Bakos, 2013). For distant observations, stellar halo measurements must sometimes be made through stacking many galaxies due to their faint brightness (Tal and van Dokkum, 2011; D’Souza et al., 2014).

Stellar halos are thought to be built at least significantly from stars and gas accreted from external sources over the course of a galaxy’s life, making the region a useful diagnostic tool for determining and analysing their formation history. This material is assembled in part through the accretion of satellite galaxies, which leave some or all of their stars in the outer halo during a merger, and also through the kinematic heating and ejection of disc stars to large radii.

As a result of the sparsity of stars in the halo, accreted material remains coherent over long timescales at large radii, remaining detectable as structures (or streams) long after accretion. Many studies have investigated

streams in the MW, for example, in order to build a coherent picture of the Galaxy's accretion history (Helmi et al., 1999; Bell et al., 2008; Grillmair and Carlin, 2016)

For those satellite galaxies which have only recently been accreted into a stellar halo, streams can be highly spatially coherent, able to be detected clearly through their positions in space. After they have dispersed and mixed, however, streams can still be detected via coherence in other parameter spaces, such as velocity, integrals of motion, and/or metallicity (e.g. Helmi et al., 1999; Kepley et al., 2007; Klement et al., 2009).

The structure and properties of the stellar halo, including the shape and stellar characteristics, can provide good evidence of formation scenarios for the Galaxy (Freeman and Bland-Hawthorn, 2002), allowing a historical picture to be built of how the Galaxy was formed.

The surface brightness or stellar density profiles of MW type stellar halos are often characterised by their power law indices, with some best fit by a single power law (e.g. M31) and others showing a break (e.g. the MW). Investigating 6 MW-mass disc galaxies, Harmsen et al. (2017) measured single power law density profiles with slopes between -2 and -3.7 along the minor axes. With such a wide range of observations of surface brightness and stellar density profiles, they make a good test for the accuracy of theoretical models.

In theoretical work, Deason et al. (2013) - using the simulations of Bullock and Johnston (2005) - investigated the density profiles of MW/M31 analogues, finding that simulated stellar halos also often (though not always) have broken power law profiles. They present evidence that the reason for a

break is related to the break radii of accreted star particle density profiles; strong breaks imply that the galaxy's accretion history is dominated by one massive satellite, or that accreted satellites have similar radii, whereas no strong break implies that the accreted stars are spread out in radius. Beers et al. (2012), on the other hand, have argued that a broken density profile is a result of a halo with two components (see Section 1.2).

Many stellar halos display a negative metallicity gradient to large radii. One of the primary causes of such a gradient is thought to be the mass-metallicity relation of accreted satellites; more massive satellites contain more metal rich stars, and can sink further into the host galaxy before being disrupted, while the less massive satellites deposit their lower metallicity stars in the outer regions of the galaxy (De Lucia and Helmi, 2008; Tissera et al., 2013). There is also a natural divide between the higher metallicity stars being formed within a galaxy at generally low radius (in situ), and the lower metallicity stars being deposited in its outer regions by satellites (accreted).

Monachesi et al. (2016a) inferred metallicity profiles from color profile measurements of 6 MW-mass disc galaxies in the GHOSTS (Galaxy Halos, Outer disks, Substructure, Thick disks, and Star clusters) survey, finding that half showed a negative gradient in their radial metallicity profile, with the others approximately flat. In parallel to this finding, the Andromeda Galaxy (M31) shows a clear negative metallicity gradient (Gilbert et al., 2014) but there is little to no evidence for a negative gradient in the MW (see Sections 1.3 and 1.2 respectively). These observations contrast with the fact that metallicity gradients of Milky-Way type galaxies in recent

theoretical studies are consistently negative.

While models which only consider accreted stars predict flat metallicity profiles (Font et al., 2006; De Lucia and Helmi, 2008; Cooper et al., 2010), cosmological simulations which also model the stellar component formed in situ overwhelmingly predict negative metallicity gradients. In the cosmological hydrodynamical GIMIC simulations (Crain et al., 2009), Font et al. (2011) found that negative gradients were ubiquitous in simulated MW-type galaxy halos, with decreases of 0.6 – 0.9 dex between the inner ($< 10\text{kpc}$) and outer ($\sim 100 - 200\text{kpc}$) halo regions. Tissera et al. (2014) simulated 6 Milky-Way mass galaxies, finding that all had negative metallicity gradients in the range $-0.008 < \Delta[\text{Fe}/\text{H}] \text{ (dex kpc}^{-1}\text{)} < -0.002$.

Theoretical metallicity profiles are usually measured through a spherical average, however observational measurements of disc galaxies are often made along a particular axis (typically the minor axis, to avoid disc contamination, e.g. Tanaka et al. 2010; Sesar et al. 2011; Gilbert et al. 2014). Monachesi et al. (2016b) propose that this may be a factor in the discrepancy between the ubiquity of metallicity gradients in simulations and the assortment of profile shapes observed in the real Universe, by showing that strong differences exist between the major and minor axis $[\text{Fe}/\text{H}]$ profiles of galaxies in the Auriga simulations.

Further work is needed to fully understand the cause of metallicity gradients, to uncover what metallicity gradients can tell us about the formation history of a galaxy, and to investigate the ongoing discrepancy between the results of observational and theoretical studies. Here we will use the EA-GLE simulations to investigate the shape and diversity of metallicity pro-

files, correlation with other properties, and proposed explanations for the inconsistency in metallicity profile results.

To gain a full understanding of stellar halos requires the use of models or simulations in order to follow their formation over billions of years, and to investigate the relative importance of different formation paths and physical processes across a range of galaxy types. Many theoretical studies analyse galaxies built up entirely from accretion events as a result of simulating only dark matter particles, using a particle tagging system to designate baryonic particles (e.g. Bullock and Johnston, 2005; Font et al., 2008; De Lucia and Helmi, 2008; Cooper et al., 2010). Such an approach is useful for investigating the effect of accretion events on a galaxy, but can introduce a number of systematic errors (Libeskind et al., 2011; Bailin et al., 2014). To fully investigate the roles played by different stellar halo components requires the use of simulations that can accurately model baryonic physics over a large volume of the Universe. Simulations of both individual high resolution galaxies and larger statistical samples are needed if we are to understand all aspects of the properties and formation histories of these galaxies.

Font et al. (2011) showed that the contribution of stars born within a galaxy (in situ stars) was an important factor when modelling stellar halos, implying that accretion only models may not be representative. This study showed that the broad properties of stellar halos can be better reproduced when in situ stars are considered. The slopes of the density and metallicity profiles were shown to be primarily driven by the change from in situ dominated ($\lesssim 30$ kpc) to accretion dominated ($\gtrsim 30$ kpc) regions.

There is also ongoing disagreement between the stellar halo fractions of theoretical models and observations, with models predicting higher stellar halo fractions as a function of galaxy mass than observed (Harmsen et al., 2017). Most notably, simulations fail to reproduce any galaxies with negligible or undetectable stellar halos. While this may indicate issues with either set of data, there is a confounding issue of halo definitions not being entirely unified. Observational definitions vary: Harmsen et al. (2017) define the stellar halo as 3x the mass measured between 10 and 40kpc (the factor of 3 comes from calibration to models), and Merritt et al. (2016) define the stellar halo as excess mass from a bulge+disk fit beyond 5 half-mass radii. In simulations, the stellar halo is often defined kinematically, separating the halo stars by their angular momentum (e.g. Font et al., 2011; McCarthy et al., 2012; Tissera et al., 2013). Studies such as Cooper et al. (2015) and Monachesi et al. (2016b) additionally remove the bulge, with a cut of $R > 5\text{kpc}$. Pillepich et al. (2015) opt for a spatial decomposition, defining the halo as those stars not contained within a cylinder enclosing the galactic disk. Though variation between some of these definitions are only distinct in the inner regions, it may be important to consider the exact definitions used when comparing results.

A large number of outstanding questions remain in the study of stellar halos: How typical are the MW and M31, and how diverse are the stellar halos of other galaxies? What is the typical fraction of a galaxy composed by its stellar halo, and how should it be defined? Does the stellar halo have two components, and if so how can they be detected? What can observational measurements of stellar halos tell us about their host galaxy's history? And

what is the source of discrepancies between stellar halo observations and simulations?

In investigating these questions we will primarily be comparing to data of the MW and M31 galaxies, alongside data of galaxies of similar mass and type, and so we provide an overview of these two galaxies here.

1.2 The Milky Way

As the galaxy in which we find ourselves, the Milky Way (MW) is a sensible place to begin when testing theoretical models against observations. In this work we will be primarily comparing the EAGLE simulations to galaxies with mass and shape similar to that of the Milky Way.

Recent virial mass estimates for the MW lie in the region (0.8 - 1.3) $\times 10^{12} M_{\odot}$ (Rashkov et al., 2013; Kafle et al., 2014; McMillan, 2017), with a stellar mass of $\sim 6 \times 10^{10} M_{\odot}$ (McMillan, 2011; Licquia and Newman, 2015).

The MW stellar halo extends beyond 100kpc - well over twice the radius of the galactic disk - and contains less than 1% ($4 - 7 \times 10^8 M_{\odot}$) of the Galaxy's total stellar mass (Bland-Hawthorn and Gerhard, 2016).

The three-dimensional shape of the MW halo is the subject of ongoing investigation. Helmi (2008) provides a good overview of the relevant studies, which are summarised here. The stellar halo density profile is often described, in a cartesian coordinate system, as:

$$\rho(x, y, z) = \rho_0 \frac{\left(x^2 + \frac{y^2}{p^2} + \frac{z^2}{q^2} + a^2\right)^n}{r_0^n} \quad (1.1)$$

where n is the power-law exponent, q is the minor-to-major axis ratio, p is the intermediate-to-major axis ratio, a is the (often left out) scale radius, and ρ_0 is the stellar halo density at a radius r_0 (typically the solar radius).

A number of surveys have attempted to parametrize the MW stellar halo density profile (Morrison et al., 2000; Robin et al., 2000; Siegel et al., 2002; Jurić et al., 2008). These surveys find values of $-3 < n < -2.4$, and $0.5 < q < 0.7$, though it is worth noting that some studies argue for parameters that change with radius, with different parameters for the inner and outer halo, and others find asymmetries with respect to the line of sight (e.g. Newberg and Yanny, 2006). Deason et al. (2011), however, find no evidence for variation with radius, and caution that evidence for triaxiality may be a result of streams.

In two dimensions, Deason et al. (2011) measured power law profiles for the MW's density profile of 2.3 (inner) and 4.6 (outer), with a break at ~ 27 kpc, and in the outer halo presented evidence for a steeper power law index of ~ 6 (Deason et al., 2014).

There is some evidence for a negative metallicity gradient across the thin and thick disk components in the MW (Ivezić et al., 2008; de Jong et al., 2010), however little to no evidence has been found for a metallicity gradient in the halo. Xue et al. (2015) find some evidence for a decreasing metallicity with radius in the outer halo, however Sesar et al. (2011) observed a consistent $[\text{Fe}/\text{H}] \sim -1.5 \pm 0.1$ dex over the radius range 10 – 40kpc.

Evidence points towards the outer ($\gtrsim 20$ kpc) halo of the MW having been primarily built via mergers (Newberg et al., 2002; Belokurov et al., 2006; Bell et al., 2008) and Deason et al. (2015) found - through the anal-

ysis of stellar population ratios - that the halo was likely built from a few massive satellites rather than many smaller ones, though there is still some evidence for a significant contribution by smaller halos (Clementini, 2010; Frebel et al., 2010). It remains unclear what fraction of the inner (or local) stellar halo was built through accretion. Through statistical arguments based on observations of nearby halo stars, Gould (2003) estimate that there could be as many as 400 streams in the inner stellar halo.

Observational and theoretical evidence has been presented arguing for a 'dual halo' in the MW. In such a model the stellar halo is built up from two distinct components with different spatial distribution, kinematics, and metallicities. Carollo et al. (2007) and Beers et al. (2012) claimed that the MW showed two such components, with the inner halo having a net prograde rotation and the outer halo a net small (or zero) retrograde rotation, though this was contested by Schönrich (2011; 2014) who argued that those studies suffered from selection biases and incorrect treatment of errors. McCarthy et al. (2012), using GIMIC, presented theoretical motivation for two distinct components, finding that galaxies in their sample often had an in situ component with some prograde rotation, alongside an accreted component with no net rotation. In recent work, Helmi et al. (2017) showed - using Gaia and RAVE data - that a significant fraction of local halo stars were travelling on retrograde orbits. An et al. (2013) found that the two components of the MW halo (prograde and retrograde) had differing metallicities, with the retrograde stars having poorer metallicity.

Rapid developments in our mapping and understanding of the MW halo have taken place with the advent of large scale surveys including SDSS,

2MASS, and QUEST (Ivezić et al., 2012). Further developments will be forthcoming with the recent and upcoming Gaia mission data releases. Data Release 1 has already resulted in a number of studies about, or with implications for, the MW halo (e.g. Deason et al., 2017; Helmi et al., 2017).

1.3 The Andromeda Galaxy (M31)

Our view of the MW is heavily restricted and obscured by our place within it. We have a much clearer view, however, of the nearby Andromeda galaxy (M31), which provides us with the opportunity for detailed study across an entire galaxy of similar mass and type as our own.

M31 has a virial mass in the range $(1 - 2) \times 10^{12} M_{\odot}$ (Tollerud et al., 2012; Fardal et al., 2013; Peñarrubia et al., 2016) and stellar mass of $(1 - 1.5) \times 10^{11} M_{\odot}$ (Barmby et al., 2006, 2007; Tamm et al., 2012). The total stellar halo mass is estimated to be $1.5 \pm 0.5 \times 10^{10} M_{\odot}$ (Ibata et al., 2014; Harmsen et al., 2017)

M31 and the MW share a number of similarities including a similar morphology and mass (Ibata et al., 2004). They are not, however, identical. M31 has a higher luminosity, higher rotation speed, and larger size (with a scale length approximately double that of the MW, Waltherbos and Kennicutt (1988); Ruphy et al. (1996))

The stellar halos of these two galaxies also suggest different formation and/or growth histories. M31 has a stellar halo mass an order of magnitude greater than that of the MW (Bell et al., 2008; Ibata et al., 2014), and a higher mean metallicity of $[Fe/H] \sim -0.7$ (Gilbert et al., 2014).

Gilbert et al. (2012) presented a surface brightness profile for M31 with no break - unlike that found in the MW - with stars following a power law with index -2.2 ± 0.2 out to ~ 175 kpc. Ibata et al. (2014) found that M31's surface brightness profile was well described by a single power-law fit, but one which became steeper with increasing metallicity, from -2.3 ± 0.02 in the range $-2.5 < [\text{Fe}/\text{H}] < -1.7$ to -3.72 ± 0.01 in the range $-1.1 < [\text{Fe}/\text{H}] < 0$.

Gilbert et al. (2014) find a continuous metallicity gradient in M31 of -0.01 dex kpc^{-1} between 9 kpc and 100 kpc, decreasing from $[\text{Fe}/\text{H}] \sim -0.4$ within 20 kpc to $[\text{Fe}/\text{H}] \sim -1.4$ beyond 90 kpc.

1.4 The EAGLE simulations

The EAGLE simulations are a suite of cosmological hydrodynamical simulations across varying box sizes (from 12 Mpc to 100 Mpc on a side), resolutions, and subgrid models; see Schaye et al. (2015, hereafter S15) for a full overview. The simulations cover a range of box sizes and subgrid parameters, from 12 cMpc to 100 cMpc on a side and 188^3 to 1504^3 particles of dark matter plus an equal contribution of baryons. Simulations are denoted as, for example, Ref-L0100N1504, which refers to a box with side length of 100 cMpc and a total of 2×1504^3 particles, with the Reference set of subgrid parameters. Reference (Ref) refers to the suite of simulations which share a common set of subgrid physics parameters and numerical techniques that best match the stellar mass function and key galaxy scaling relations. The Recalibrated (Recal) simulations have had their subgrid stellar and AGN

feedback parameters calibrated again as a result of resolution changes.

The EAGLE simulations assume cosmological parameters from Planck Collaboration I (2014) and Planck Collaboration XVI (2014); $\Omega_m = 0.307$, $\Omega_b = 0.04825$, $h = 0.6777$, and $\sigma_8 = 0.8288$. Initial conditions using these parameters were adopted (see S15 for full details), and the simulations were evolved by a modified version of the N -body TreePM smoothed particle hydrodynamics (SPH) code GADGET3 (Springel, 2005). Data was output at two time resolutions: 29 'snapshots' were recorded between redshifts 20 and 0, with a reduced set of data recorded in 'snipshots' at 400 redshifts over the same range.

Galaxies and their halos are identified by first using a friends-of-friends (FoF) algorithm (Davis et al., 1985) on the dark matter particles, with stars, gas, and black holes (BHs) associated to the FoF group of their nearest dark matter particle. Subhaloes are then identified, using all particle types, in these FoF groups using the SUBFIND algorithm (Springel et al., 2001; Dolag et al., 2009). The central subhalo is defined as that containing the particle with the minimum gravitational potential. This is typically the most massive subhalo, and thus can generally be considered as the galaxy, while non-central subhalos belonging to the FoF group can be considered as satellite or merging galaxies.

The EAGLE simulations have been successful in reproducing a wide range of observable galaxy properties, including their colours and bi-modality (Trayford et al., 2015, 2016), the evolution of both the stellar mass function (Furlong et al., 2017) and galaxy sizes (Furlong et al., 2015), and the co-evolution of stellar mass, SFR, and gas (Lagos et al., 2016).

Table 1.1: Box size, particle number, baryonic and dark matter particle mass for the EAGLE simulations used in this work.

Simulation	L (cMpc)	N	m_g (M_\odot)	m_{dm} (M_\odot)
L0100N1504	100	$2 \times (1504)^3$	1.81×10^6	9.70×10^6
L0050N0752	50	$2 \times (752)^3$	1.81×10^6	9.70×10^6
L0025N0752	25	$2 \times (752)^3$	2.26×10^5	1.21×10^6
L0025N0376	25	$2 \times (376)^3$	1.81×10^6	9.70×10^6

Table 1.2: Values of the subgrid parameters that were varied in models used here. f_{th} controls the feedback efficiency and its dependencies, C_{visc} defines the black hole accretion disc viscosity, and ΔT_{AGN} the AGN feedback energy.

Prefix	f_{th} -scaling	$f_{th,min}$	$f_{th,max}$	$C_{visc}/2\pi$	ΔT_{AGN} \log_{10} (K)
FBConst	-	1.0	1.0	10^3	8.5
FB σ	σ_{DM}^2	3.0	0.3	10^2	8.5
FBZ	Z	3.0	0.3	10^2	8.5
Reference	Z, ρ	0.3	3	10^0	8.5
AGNdT8	Z, ρ	0.3	3	10^0	8.0
AGNdT9	Z, ρ	0.3	3	10^0	9.0
StrongFB	Z, ρ	0.6	6	10^0	8.5
WeakFB	Z, ρ	0.15	3	10^0	8.5

This work primarily investigates the Recal-L0025N0752 and Ref-L0100N1504 runs. Recal-L0025N0752 has double the resolution per side compared to Ref-L0100N1504, giving approximately 8 times the number of particles per galaxy, allowing for high-resolution investigation with the caveat of fewer galaxies due to the smaller box size. Ref-L0100N1504 allows the study of a broader population of galaxies at the expense of individual detail. In addition, Recal-L0025N0752 has been shown to produce a galaxy mass-metallicity relation in better agreement with observational data (S15), particularly at lower stellar masses ($M_* \lesssim 10^{10} M_\odot$), as a result of its higher

feedback efficiency. This makes it the best choice for investigating EAGLE’s MW-type stellar halos, a large fraction of which are built from low mass satellites.

Table 1.1 provides details, including particle masses, for the main simulation runs used here.

1.4.1 Subgrid physics

In addition to the reference and recalibrated model variations, simulations with modified subgrid processes were also run to explore the sensitivity of results to the variation of these parameters (S15). The key subgrid parameters involved in the variations analysed here are detailed in Table 1.2.

Star formation feedback efficiency is controlled by the f_{th} parameter; $f_{th} = 1$ corresponds to an injected energy of 1.736×10^{49} erg M_{\odot}^{-1} per stellar mass formed. Hydrodynamical simulations provide an opportunity for this feedback parameter to be specified based on the conditions local to a star particle. Four primary feedback calibrated simulations were run for EAGLE, with the first specifying a constant f_{th} and the other three varying in the range $0.3 < f_{th} < 3$ based on local properties:

- *FBconst* uses a fixed quantity of energy per unit stellar mass formed (i.e. $f_{th} = 1$ for all star particles); while this model reproduces the observed $z = 0.1$ Galactic Stellar Mass Function (GSMF), it fails to reproduce the observed sizes of disc galaxies.
- *FB σ* scales f_{th} as a function of σ_{DM}^2 , the velocity dispersion of dark matter particles near the star particle, a proxy for the characteristic

virial scale of the particle’s environment. This is motivated by the corresponding effect of maximising the feedback efficiency in low-mass galaxies while reducing it in massive galaxies. In order for this model to fit the $z = 0.1$ GSMF, a higher subgrid viscosity for BH accretion was required.

- *FBZ* provides a physical basis for varying f_{th} , adjusting it with respect to the local metallicity (Z). The effect is similar to that in *FB σ* , with star particles in low mass galaxies having a greater feedback efficiency due to the galactic mass-metallicity relation.
- *Ref* (or *FBZ ρ*) provides a scaling dependent on both the local metallicity and the density of the star’s progenitor gas particle, providing a scaling relation with a form similar to that of *FBZ*, but stars formed from higher (lower) density gas have a greater (lesser) feedback efficiency. This form overcomes numerical losses present in the *FB σ* and *FBZ* models.

Two models with more extreme feedback were also run, varying the Ref-L0025N0376 model with much weaker and stronger feedback efficiency, scaling the feedback function by 0.5 and 2. The WeakFB model adopted an efficiency of $0.15 < f_{th} < 0.6$ and StrongFB an efficiency of $1.5 < f_{th} < 6$. The median efficiency of all star particles formed prior to $z = 0.1$ in the WeakFB, Ref, and StrongFB models are 0.38, 0.63, and 1.22, respectively.

All EAGLE halos with a mass greater than $10^{10}M_{\odot}$ contain a BH, which is created from the highest density gas particle upon the halo reaching the mass threshold. The BH accretes material over time through a subgrid

model of an accretion disc. The viscosity of this accretion disc is set by the C_{visc} parameter, which controls the Bondi-Hoyle (1944) accretion rate; higher C_{visc} corresponds to a lower viscosity, slowing the growth of BHs. The EAGLE reference model uses $C_{visc}/2\pi = 1$, and variations of $C_{visc}/2\pi = 10^2$ (ViscLo) and $C_{visc}/2\pi = 10^{-2}$ (ViscHi) were run.

The energy of the subsequent Active Galactic Nuclei (AGN) is determined primarily by the ΔT_{AGN} parameter. A larger value of ΔT_{AGN} results in more energetic feedback events but makes the feedback more intermittent. The reference model uses $\Delta T_{AGN} = 10^{8.5}K$, and variations of $\Delta T_{AGN} = 10^8K$ (AGNdT8) and $\Delta T_{AGN} = 10^9K$ (AGNdT9) were also run; S15 found that AGNdT9 reproduced more accurately the gas fractions and luminosities of galaxy groups.

Chapter 2

Stellar halos in EAGLE

In this study the EAGLE simulations are used to investigate the properties of the stellar halos of galaxies of Milky Way (MW) mass and type.

One of the tests that the EAGLE simulations can be used to reliably describe the formation history of galaxy stellar halos is to ascertain that the properties of present day stellar haloes match those of the observed haloes of galaxies. To investigate whether EAGLE reproduces observable properties of stellar halos, we start by analysing galaxies with properties similar to the MW and Andromeda (M31). These are among those galaxies with the best available data with which to compare to. We will also compare our simulated halos with those of other galaxies of similar mass and morphology.

2.1 Galaxy selection

The EAGLE simulations were not designed to reproduce the local group (unlike, e.g., Fattahi et al., 2016), and so no galaxy exactly represents the

MW. We therefore select galaxies with properties similar to those of the MW. Here we use a selection criteria of total halo mass and circularity. The primary criterion is a mass cut in the present day total (gas+stars+DM) mass within r_{200} (the radius enclosing a mean density of 200 times the critical density of the universe at $z = 0$). We use a mass range of $7 \times 10^{11} < M_{200} < 3 \times 10^{12} M_{\odot}$ to encompass the literature mass estimates for the MW and M31 (Karachentsev and Kashibadze, 2006; Guo et al., 2010; Boylan-Kolchin et al., 2013; Fardal et al., 2013). We apply this mass range cut to the FoF mass (which includes the central galaxy and substructure) but do not include bound substructure in the rest of the analysis presented here when referring to the galaxy. After the mass cut the L0100N1504 and L0025N0752 samples contain 1313 and 35 galaxies, respectively.

Unless otherwise noted, galaxies are aligned to have their stellar disc on the x-y plane, by choosing the z-axis to align with the total angular momentum of stars within 15% of the galaxy’s virial radius (typically around 35kpc). This cut is used to remove outer structures which may have been recently accreted, such that the alignment primarily affects the disc and bulge regions.

To select disc galaxies from our sample, we first follow the approach of Stinson et al. (2010), which is based on the method of Abadi et al. (2003), to denote stars as belonging to either the disc or spheroid. With the stellar disc aligned perpendicular to the z-axis, we calculate the angular momentum of each star particle perpendicular to the $x - y$ plane, J_z , and compare it with the angular momentum of a star particle on a corotating circular orbit at the same radius, J_{circ} . Whereas in Abadi et al. (2003) stars can only

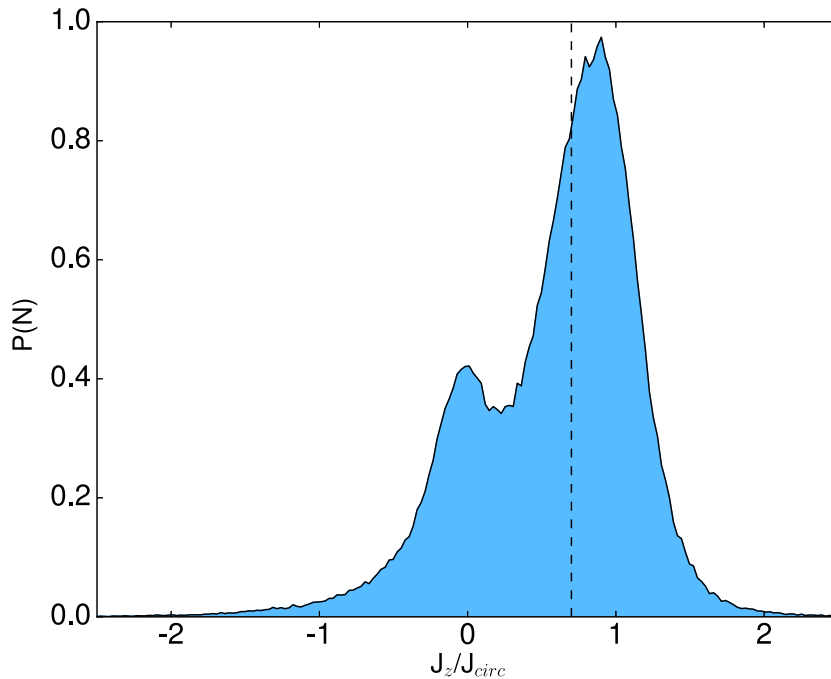


Figure 2.1: The probability distribution of J_z/J_{circ} for one galaxy from the L0025N0752 sample. The dotted line denotes $J_z/J_{circ} = 0.7$, which is used as our cut for separating disc and spheroid stars.

have $J_z/J_{circ} \leq 1$, the values here can extend beyond this limit because this method assumes a simple spherically symmetric potential. We find that there is no significant difference between this method and the similar definition used by Sales et al. (2010) where stars are instead categorised by their circular kinetic energy.

Figure 2.1 shows an example J_z/J_{circ} distribution for a galaxy from the L0025N0752 sample. Disc stars are defined with a cut of $J_z/J_{circ} > 0.7$, and spheroid with $J_z/J_{circ} < 0.7$. In addition to this, we follow Cooper et al. (2015) and approximately split the spheroid into halo and bulge components

through a separation at 5kpc. This decomposition is not perfect - it is certainly not the case that such hard divides separate the halo and disc or halo and bulge stars. Overlapping Gaussians are likely to be more accurate. Nevertheless, this simple decomposition appears to work well visually to separate the disc and halo.

From these stellar classifications we then use the disc-to-total (where total is total stellar mass) mass ratio (D/T) to select disc galaxies, using a criterion of $D/T > 0.4$ (i.e. composed of greater than 40% disc stars). The exact D/T cut is largely arbitrary, though Font et al. (2011) - studying the GIMIC simulations - used cuts of 0.2, 0.3, and 0.4, and found that none of their results changed substantially. Visually, using $D/T > 0.4$ for our galaxy sample worked best to select galaxies with a clear disc, that are generally not currently undergoing a major merger, and that had been aligned correctly to the x-y plane (see Figure 2.2). Visually, the vast majority of galaxies are correctly aligned, with just a few which appear to be mildly off-axis, likely due to recent accretion events. Following the D/T cut, the samples contain 9 galaxies (26%) in Recal-L0025N0752 and 352 (27%) in Ref-L0100N1504. Details of the average properties of these galaxies are shown in Table 2.1.

While the MW is not thought to have undergone any recent major mergers, we do not set any constraint on the merger history of the galaxies selected here beyond the side effect of the D/T cut, which tends to exclude galaxies that have recently undergone a major merger.

Figure 2.3 shows the range of galaxy masses and virial radii for the two simulation runs before and after applying the morphology cut. The left column shows the number of galaxies for each simulation in bins of virial

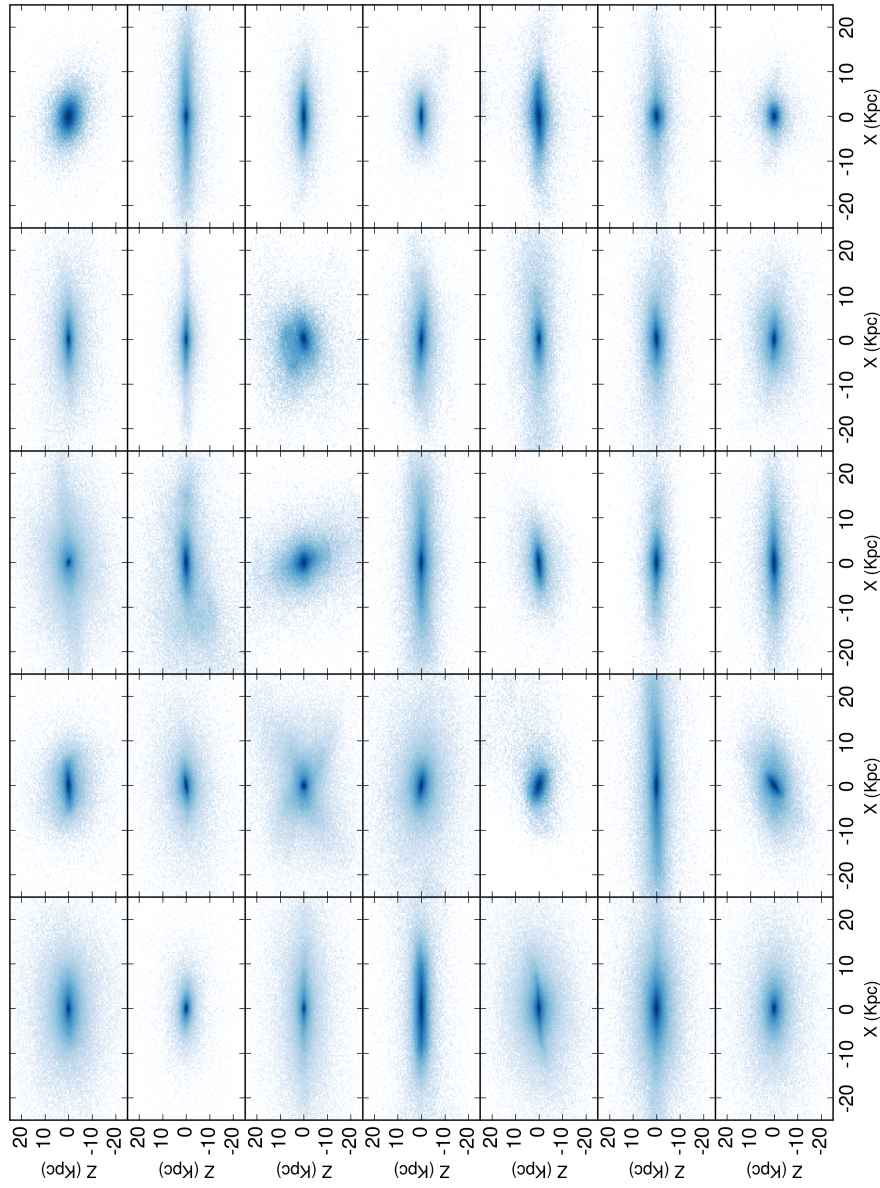


Figure 2.2: Edge-on density maps for the 35 galaxies selected by the mass cut from the L0025N0752 simulation. ϵ (J_z/J_c) values are denoted for each galaxy.

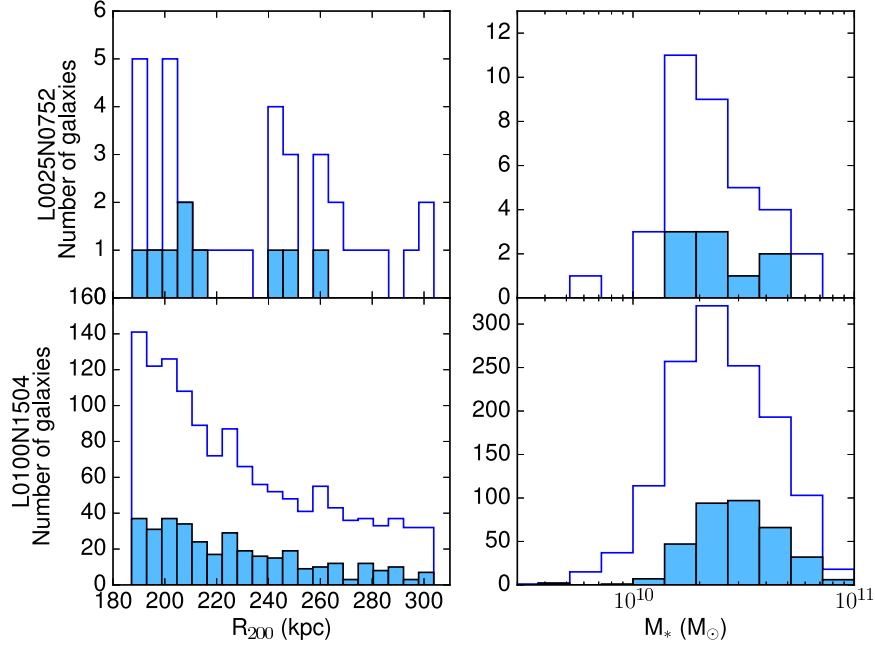


Figure 2.3: Virial radius (R_{200} , left) and stellar mass (right) distributions for the two galaxy samples presented here. Dark blue line and shaded region represent the galaxy sample before and after applying the cut of $D/T > 0.4$ respectively.

radius (R_{200}), and the right in bins of total stellar mass. The D/T cut does not substantially alter the distribution of galaxies in terms of their radius or mass.

2.2 Separating accreted and in situ stars

To investigate stars in stellar halos in detail it is useful to split the population into two categories: those stars born within the central galaxy (in situ), and those accreted through mergers. We first generate lists of dark matter

Table 2.1: Mean stellar mass, virial radius, number of star particles, and metallicity for systems selected by the mass and morphology cuts.

Simulation	\bar{M}_* (M_\odot)	R_{200}^- (kpc)	\bar{N}	$\langle[\text{Fe}/\text{H}]\rangle$
L0100N1504-Ref	3.25×10^{10}	227	24585	-0.24
L0025N0752-Recal	2.47×10^{10}	219	155120	-0.35

particles for each galaxy’s FoF group, and use the unique particle IDs to find the FoF group in the previous output (snapshot or snipshot) that contains the largest fraction of these particles, defining it as the progenitor. Using this history of most massive progenitors, we can then go back through the outputs to define our populations of in situ and accreted star particles. The birth location of star particles is defined as the location of the gas particle from which they formed in the last output before they became a star. Stars born within the most massive subhalo of the FoF group (i.e. the central galaxy) are defined as in situ, and all other stars are defined as accreted.

We make no further distinctions within these groups, such as splitting the accreted group into those stars accreted smoothly or through a satellite, nor whether the accreted star formed inside the satellite pre or post-infall, but note that such sub-classifications can be informative (e.g. Pillepich et al., 2015).

While with the L0025N0752 simulation we have the benefit of high time resolution snipshots (over 400 outputs, see Section 1.4) for defining stellar birth locations, for the L0100N1504 simulation the snipshots would be prohibitively time consuming to process in this way. As our definition could be greatly affected by the time resolution of our data, we first verify that snapshots are able to correctly isolate accreted stars from those born in

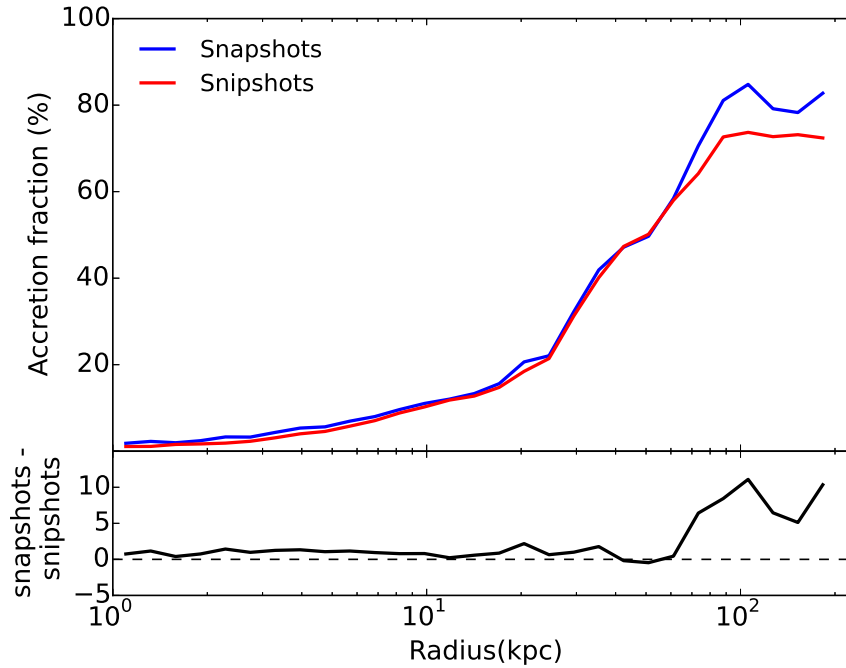


Figure 2.4: Median accretion profiles for the L0025N0752-Recal galaxies, showing the fraction of stars present at $z = 0$ that were born outside the central galaxy in radial bins. The red line shows the profile generated by using high time resolution snipshots, and the blue line shows the profile generated using the lower time resolution snapshots. Bottom panel shows the difference in fraction of accreted particles detected with each data set.

situ by generating accretion profiles for both snipshots and snapshots for the L0025N0752 simulation. Examining all galaxies in the sample we find that snipshots and snapshots show mean accreted fractions (the fraction of stars in the central galaxy at $z = 0$ which were accreted) of 12% and 13%, respectively.

Figure 2.4 shows the median accretion profile in radial bins for selected galaxies in the L0025N0752 simulation for both snapshots and snipshots,

which can be read as low and high time resolution respectively. While snapshots show a consistently higher fraction of accreted stars, the difference is negligible out to around 60kpc. At radii greater than 60kpc the snapshots misidentify up to around 10-15% of stars as accreted. Given that the overall increase is low (1%), and that stars misidentified as accreted will be those formed from gas recently accreted through a merger,¹ we do not consider this to be a hindrance for defining accreted stars in L0100N1504 using only the snapshots.

2.3 Density and surface brightness profiles

Figure 2.5 shows surface density profiles (with the disc oriented face-on) for the L0100N1504 galaxy sample along with observational data of MW mass galaxies M81 ($M_* \sim 10^{11} M_\odot$), NGC 2403 ($M_* \sim 10^{10} M_\odot$), NGC 1087 ($M_* \sim 10^{10.4} M_\odot$), and NGC 7716 ($M_* \sim 10^{10.5} M_\odot$). The EAGLE galaxies agree well with NGC 1087 and NGC 7716 out to large radii, though the density profile of NGC 2403 drops to lower values compared to the EAGLE data set beyond ~ 10 kpc. M81 is close to the density profile of the highest mass galaxies of our sample (grey line), which is to be expected given that its mass is at the high end of our selected mass range; likewise for NGC 2403 dropping to lower densities and being at lower mass. The median

¹It is possible that in one data output a gas particle is in a satellite galaxy which is being accreted onto a central. Between outputs, this gas is accreted into the central, and some time before the next output, becomes a star particle. Because of the way accreted particles are defined here, the last known location of the particle is used; the star is defined as having been formed in the satellite galaxy rather than the central and is therefore misclassified as accreted. Higher time resolution lessens this effect, and thus reduces the accretion fraction to more accurate levels.

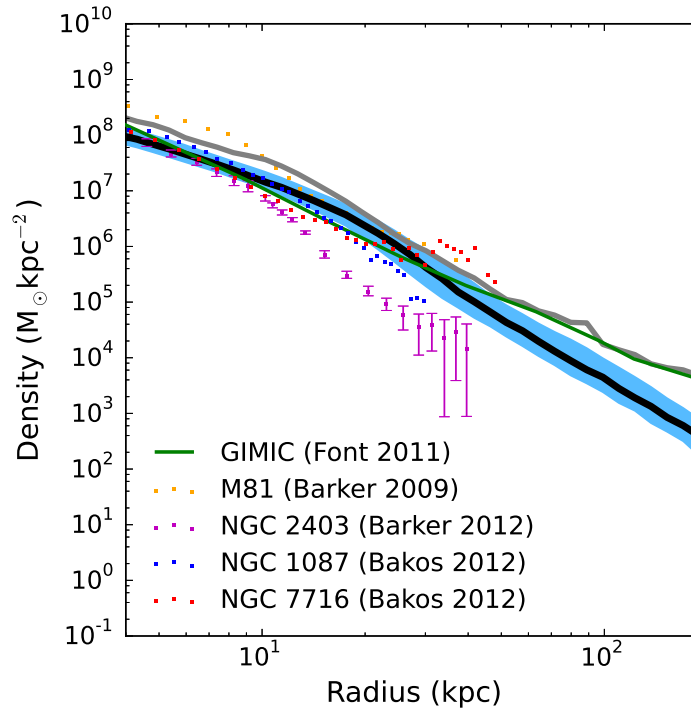


Figure 2.5: Median face-on surface density profile for the L0100N1504-Ref galaxy sample, taken along the x-y galaxy plane. Blue shaded region denotes the 25th and 75th percentiles. The grey line represents the highest mass galaxy in our sample. Also shown is data from the GIMIC simulation (Font et al., 2011) and observational data of Milky-Way mass galaxies from Barker et al. (2009, 2012) and Bakos and Trujillo (2012)

profile has a break at ~ 20 kpc, with the inner profile following a power law of $\alpha = -2.1 \pm 0.5$ and the outer $\alpha = -4.0 \pm 0.8$ (Figure 2.6), keeping the break radius density fixed. These indices are shallower than but consistent with those measured for the MW by Deason et al. (2011).

Interestingly, the galaxies in the GIMIC simulation have a density profile of a different shape than found here, with no obvious break and a signifi-

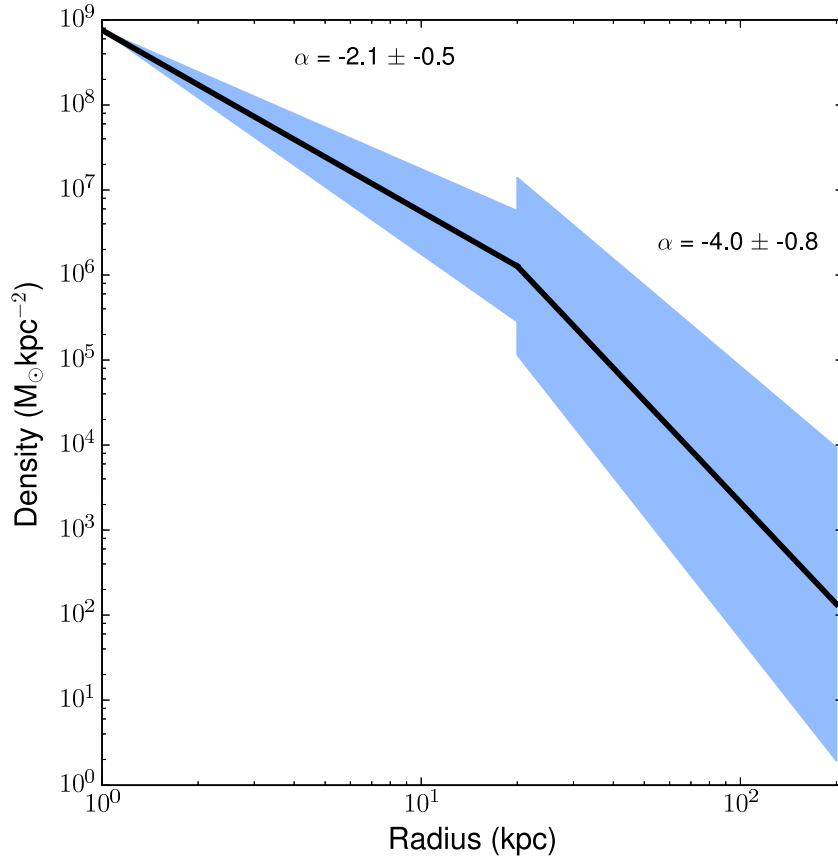


Figure 2.6: Broken power law fit to the median surface density profile shown in figure 2.5 with a break radius of 20kpc. Blue shaded region bounds the power law errors.

cantly higher density at large radius.

Star particles were assigned luminosities by modelling simple stellar populations for each star particle based on their mass, age, and metallicity. From these luminosities, stellar brightness profiles can be derived.

Figure 2.7 shows surface brightness profiles of the L0100N1504 galaxy

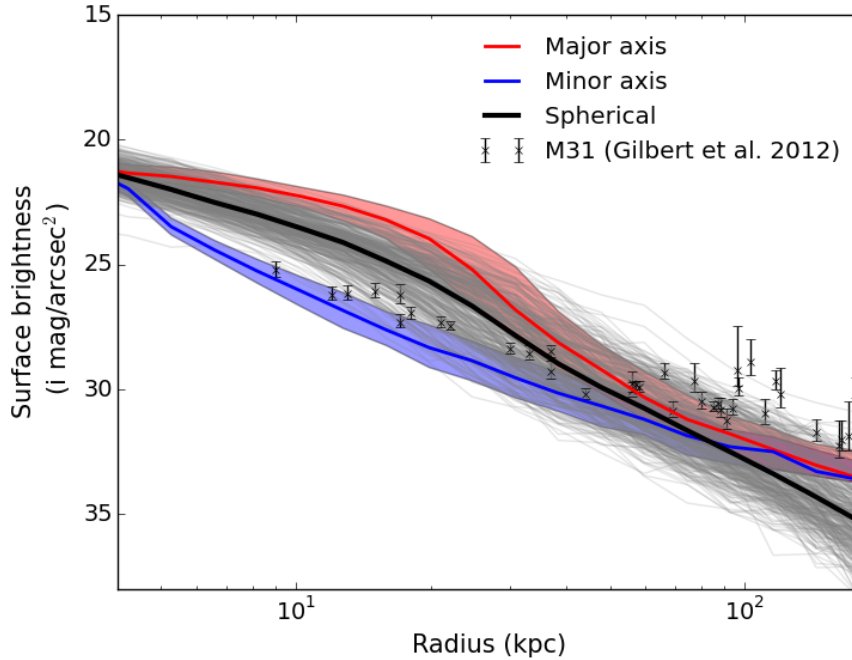


Figure 2.7: Surface brightness profiles in the i band. The red and blue lines are the surface brightness profile along the major and minor axes respectively. Also shown is surface brightness data of M31 from Gilbert et al. (2012).

sample, including the spherical average, and along the major and minor axes. Observational data of M31’s minor axis from Gilbert et al. (2012) are super-imposed. M31’s minor axis surface brightness data are within the range of our galaxy sample, and has a similar slope to that measured along the minor axis of our galaxy sample, though slightly brighter overall.

2.4 Metallicity distribution

As described in Section 1.1, the stellar halo metallicity profile is a topic of ongoing research, with some disagreement regarding the ubiquity of negative metallicity gradients. To analyse this topic in detail, we first compute the metallicity of each star particle as the logarithm of the ratio of its iron-to-hydrogen mass fraction to that of the Sun (taken to be 0.00156, Guzik et al. 2005).

The median metallicity distribution of the two MW-mass galaxy samples are shown in Figure 2.8, along with the distributions split into inner ($< 30\text{kpc}$) and outer ($> 30\text{kpc}$) regions. The outer galaxy regions are clearly of lower metallicity, with significantly less high metallicity and more low metallicity stars. The median $[\text{Fe}/\text{H}]$ for all stars is -0.35 and -0.24 for the L0025N0752 and L0100N1504 runs respectively, with the inner region having a median of -0.31 and -0.21 and outer region -0.71 and -0.75 . The lower metallicity of the inner region in the L0025N0752 sample is likely a result of the higher recalibrated stellar feedback efficiency.

Figure 2.9 shows the median spherically averaged metallicity profile and scatter about the median for both galaxy samples. The mean of metallicity in radial bins is computed to generate spherically averaged metallicity profiles for each galaxy. The median profiles are then the median of all profiles in each bin. Also plotted are the measurements for M31 (with tidal debris removed) by Gilbert et al. (2014).

As in the GIMIC simulation (Font et al., 2011), we find that metallicity gradients are a universal feature of the simulated galaxy population. The

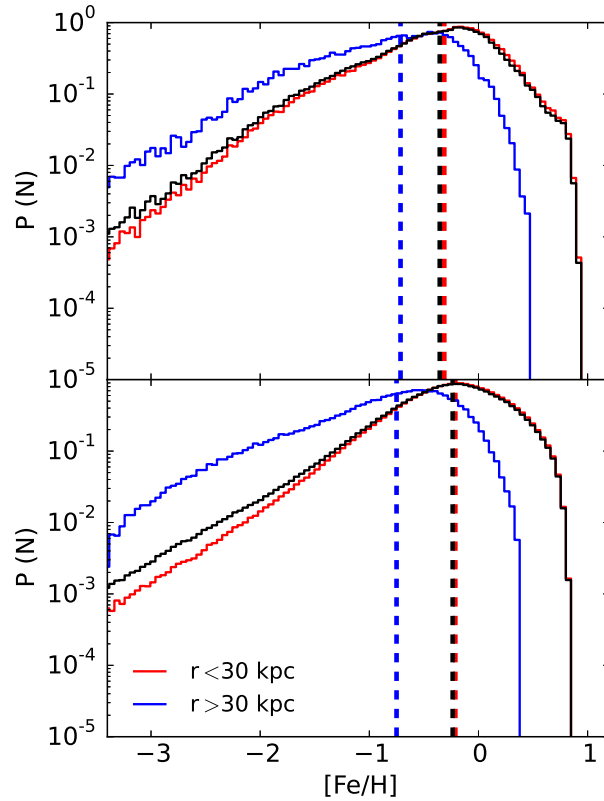


Figure 2.8: Median metallicity distribution functions for the L0025N0752 (top) and L0100N1504 (bottom) galaxy samples. Black line denotes all stars, red is the inner region of the galaxy (< 30 kpc), and blue is the outer region (> 30 kpc). The dotted lines note the median for each region.

metallicity of these galaxies decreases continually from $[Fe/H] = 0 - 0.5$ dex down to nearly -1.5 , and agrees well with the observational data of M31. The metallicity and metallicity gradient of the outer (> 30 kpc) galaxy regions are consistent between the two simulated samples, though the inner regions are of higher metallicity in L0100N1504.

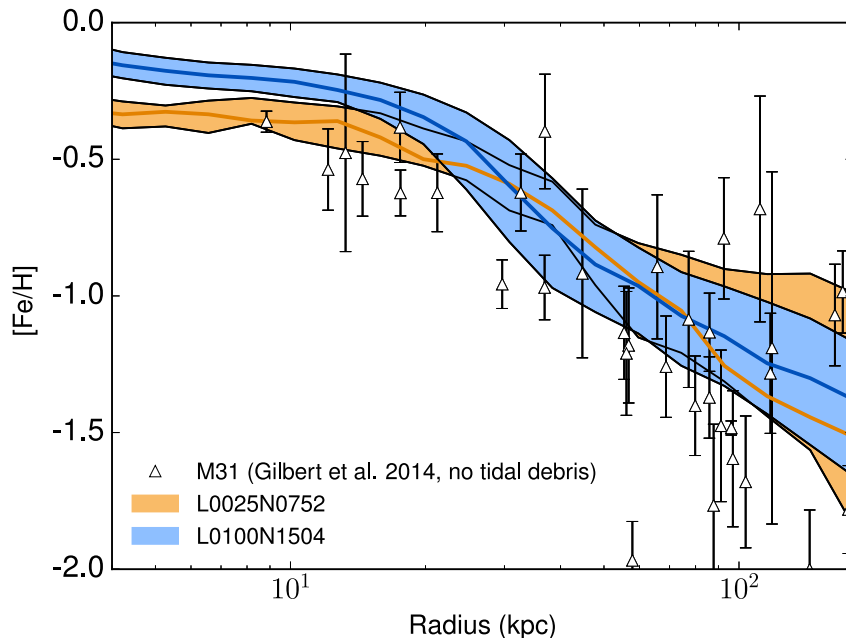


Figure 2.9: Median spherically averaged stellar metallicity profile for galaxies in the L0100N1504 and L0025N0752 simulations. Solid lines denote the median stellar metallicity profile for all stars, and the shaded region encloses the 25th and 75th percentiles. Black triangles represent the M31 metallicity measurements of Gilbert et al. (2014) with tidal debris removed.

The ubiquity of metallicity gradients in the EAGLE simulations is further demonstrated in Figure 2.10. This shows the distribution of metallicity gradients for the 352 MW-mass galaxies in the L0100N1504 simulation. Gradients were measured using a simple linear fit between 10 and 90kpc for comparison with Gilbert et al. (2014). We find that measuring gradients out to 200kpc does not change the results substantially. It is clear that all galaxies in our sample have an overall negative metallicity gradient, ranging between -0.002 and -0.02 dex kpc^{-1} . The metallicity gradient (between 10

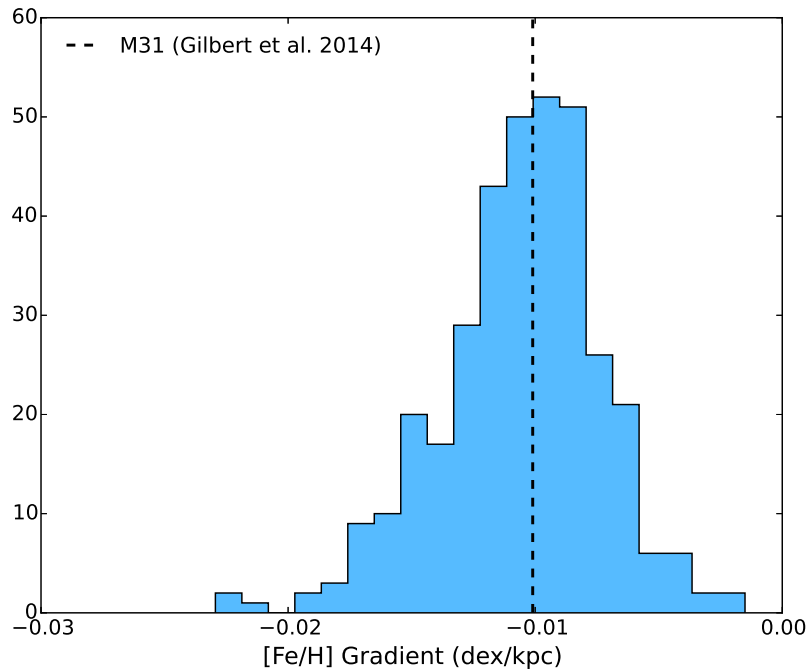


Figure 2.10: Distribution of metallicity gradients for galaxies in the L0100N1504 Reference simulation. Gradients are measured with a linear fit between 10 and 90kpc. Black dashed line is the gradient determined for M31 from Gilbert et al. (2014).

and 90kpc) in M31 is -0.0101 dex/kpc, as measured by Gilbert et al. (2014). This is shown in Figure 2.10 by the dashed line, positioned close to the mean gradient value from EAGLE. In Section 2.6 we show that the metallicity gradient is strongly affected by the stellar feedback efficiency used in the simulations.

While the L0100N1504 simulations can shed light on global properties of these galaxies, mean and median profiles hide the detailed system-to-system variation in metallicity profile shapes. Figure 2.11 shows individual

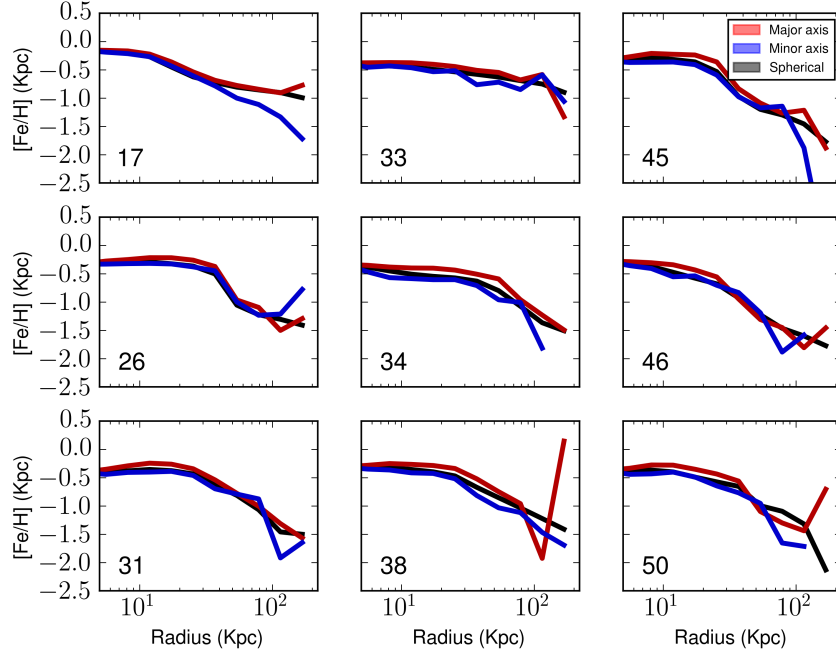


Figure 2.11: Individual metallicity profiles for galaxies in the L025N0752-Recal sample. Black line is spherically averaged, red and blue lines are the profile as measured along a 8kpc wide major and minor axis mask respectively. Sharp peaks or dips at high radius are a result of low number statistics.

metallicity profiles for the 9 MW-mass disc galaxies in the higher resolution L0025N0752 run. Here, a large variation in profile shapes can be seen, with some galaxies declining in metallicity over their entire radial range, and others with flatter profiles and a sharp drop. Metallicity profiles as measured along 8kpc wide strips positioned along the major and minor axes of the galaxy are also shown. While stars along the major axis are consistently more metal rich than on the minor axis, the difference is small, and does not lead to a substantial difference in the measured metallicity gradient.

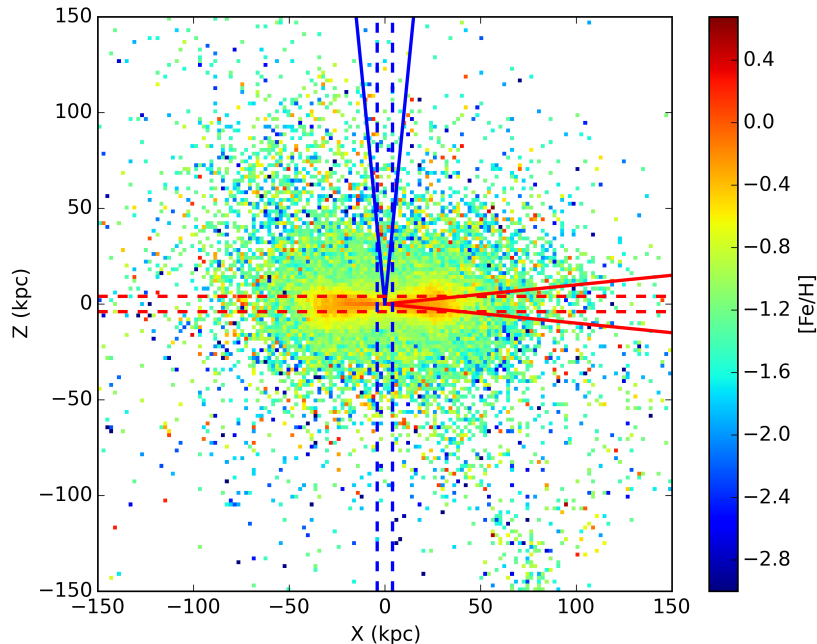


Figure 2.12: Metallicity ($[\text{Fe}/\text{H}]$) map for galaxy 26 from the L0025N0752-Recal galaxy sample, with the galaxy viewed edge on. Red and blue lines denote major and minor axes masks respectively, with solid lines bounding the 'wedges', comparable to that used by Monachesi et al. (2016b), and dashed lines bounding the 'blocks' used for major and minor masks used in this work. It is clear that the highest metallicity stars are found in the center, with metal poor stars outside.

Monachesi et al. (2016b), carrying out a similar analysis on the Auriga simulations, found that measurements along a galaxy's minor axis gave a considerably flatter metallicity profile with lower median $[\text{Fe}/\text{H}]$ values (as much as 0.4 dex) as compared to a spherically averaged one.

One possible reason for the discrepancy between those results and this work is the definition used for axes measurements. Here we use a mask 8kpc wide at all radii for consistency with typical observational studies, whereas

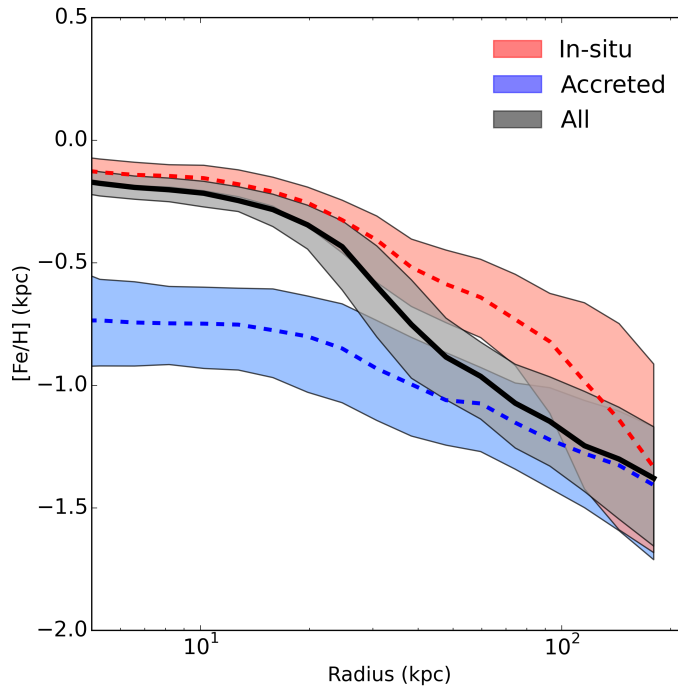


Figure 2.13: Median spherically averaged stellar metallicity profile for the L0100N1504 sample, also showing in red and blue the profiles when limited to stars born in situ and accreted respectively. Shaded regions indicate the 25th and 75th percentiles.

Monachesi et al. (2016b) use wedges widening with increasing radius from the galactic centre (see Figure 2.12). Using wedges of similar size on the galaxy sample presented here does further separate the major and minor axis $[\text{Fe}/\text{H}]$ values, but still does not result in a flattened metallicity profile or significantly different metallicities for either.

Splitting all stars (bulge, disc and halo) into accreted and in situ components can shed light on the origin of the metallicity gradient. In Figure

2.13 median spherically averaged metallicity gradients for the in situ and accreted components are presented. While both components consistently decrease with radius, the in situ component does so with a larger gradient. The primary reason is the increasing fraction of stars that are accreted versus in situ with radius (Figure 2.4), causing the overall profile to move from the high in situ metallicities within $\sim 30\text{kpc}$ to being dominated by the low accreted metallicities beyond $\sim 70\text{kpc}$. While this provides some explanation for the overall trend, it does not explain why the in situ profile itself still has a negative gradient.

2.5 Subgrid physics

We conduct much of the same analysis as in the previous sections for the L0050N0752 subgrid model variations to investigate the stellar halos' sensitivity to the varied parameters. The AGN temperature and accretion viscosity parameters do not significantly alter the metallicity or density profiles of the outer regions of these galaxies, implying that AGN feedback strength is largely unimportant to the structure of the halo.

Figure 2.14 shows the median metallicity and density profiles for the L0050N0752 *FBconst*, *FB σ* , *FBZ*, and *Ref* model variations (described in Section 1.4.1). In the top panel the median spherical metallicity profile is shown (using the same method as described in Section 2.4) for each feedback run. The *Reference* run has the highest metallicity at all radii, most likely as a result of its low median feedback efficiency (as compared to the other runs), resulting in more metal-rich gas being retained within galaxies. The bottom

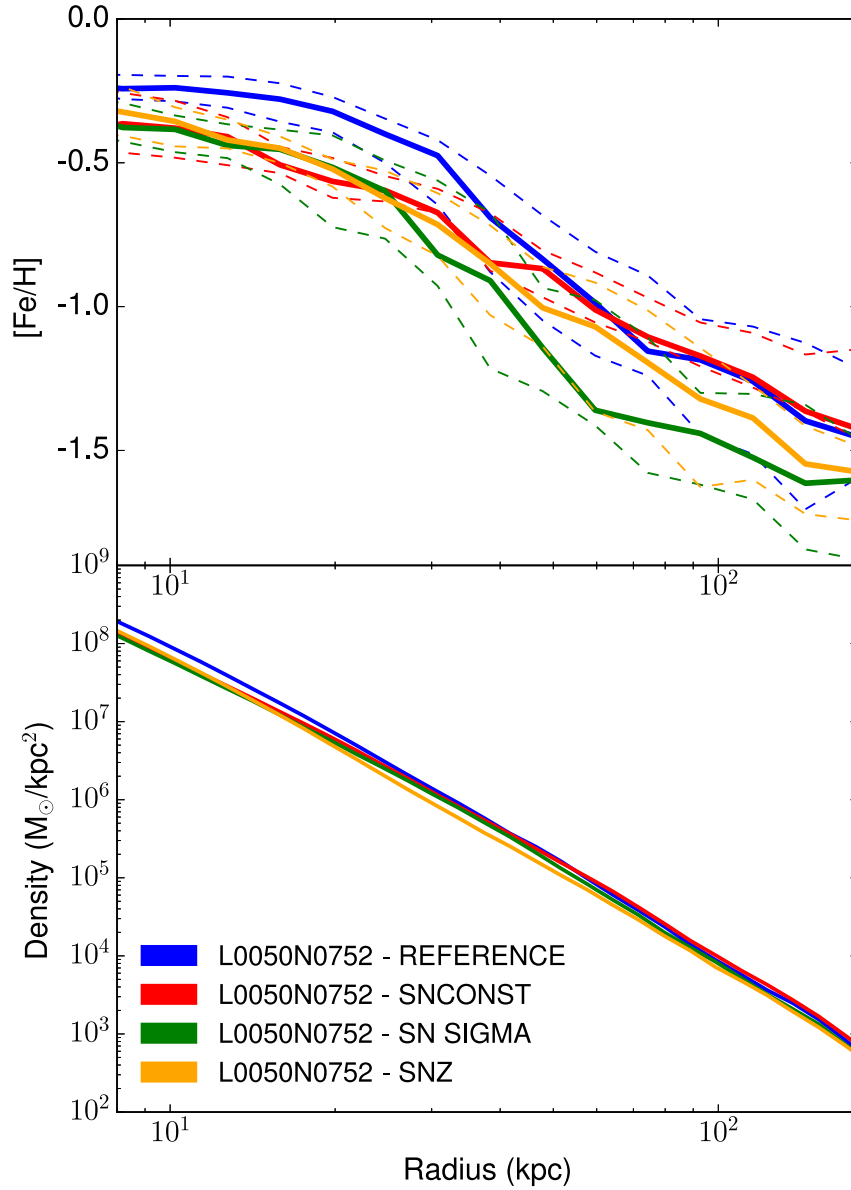


Figure 2.14: Metallicity and density profiles for the L0050N0752 model variation galaxy samples. *Top*: Median spherically averaged $[\text{Fe}/\text{H}]$ profiles. Dotted lines denote 25th and 75th percentiles. *Bottom*: Surface density profiles.

panel shows surface density profiles for each model. These are considerably more similar, except in the inner regions where galaxies in the *Reference* model have higher densities.

2.6 Halo dependence on substructure

Figure 2.15 displays the mass-metallicity relation for redshift zero satellites for both the L0025N0752 and L0100N1504 galaxy samples. Also shown is observational data in the relevant mass range from SDSS observations by Gallazzi et al. (2005) and for dwarf galaxies from Kirby et al. (2013). The metallicity of EAGLE’s satellite galaxies is consistently higher than the observed samples at all mass ranges (though note that S15 find better agreement at higher masses than investigated here), though L0025N0752 is a considerably better match below $M_* = 10^{9.5}M_\odot$ as a result of the higher feedback efficiency acquired through recalibration.

No correlation was found between the gradient of the mass-metallicity relation of a galaxy’s $z = 0$ satellites² and the strength of its radial metallicity gradient, even when limiting measurement of the metallicity gradient to the accreted population.

We also test for correlation using two extreme models - the L0025N0376 WeakFB and StrongFB runs, which effectively scale the feedback efficiency of the reference model by 0.5 and 2 respectively (see Section 1.4.1 for details). While these runs do not form realistic galaxies in the same sense as

²As measured by a simple linear fit, limited to galaxies with more than 5 satellites of mass $>10^7M_\odot$. This mass limit was chosen as satellites/subhalos less massive will only be composed of a maximum of 10 stars in the L0100N1504 case.

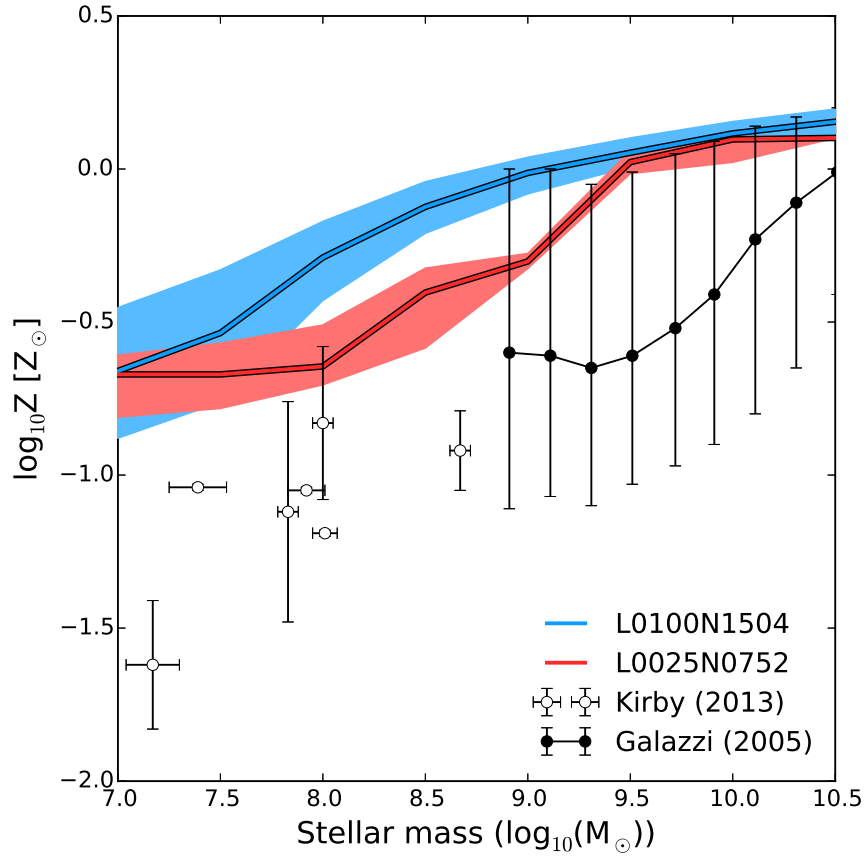


Figure 2.15: Stellar mass-metallicity relation for the $z = 0$ satellites of each galaxy sample. Blue denotes the L0100N1504 sample, and red the L0025N0752 sample. Also plotted is observational data of galaxies from Galazzi et al. (2005) and Kirby et al. (2013)

the other runs analysed here, in particular because they do not form disc galaxies selectable by the criteria used for L0100N1504 and L0025N0752 (we instead take all galaxies in the mass range), they are useful for clearly uncovering the feedback dependency of broad galaxy properties. Figure 2.16

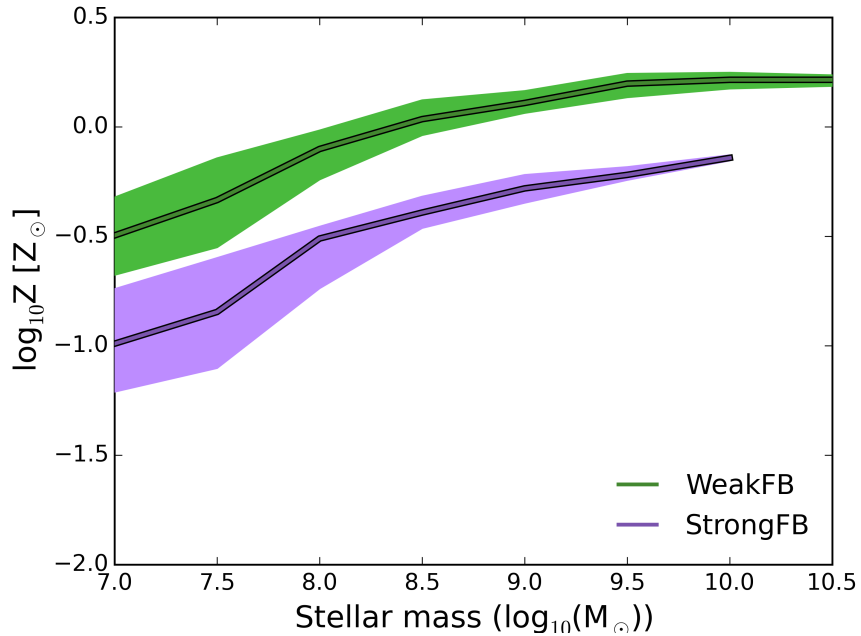


Figure 2.16: Median stellar mass-metallicity relation for the $z = 0$ satellites of the two extreme feedback runs. Green denotes the WeakFB sample, and purple StrongFB. The shaded region encloses the 25th and 75th percentiles.

shows the mass-metallicity relation of galaxy satellites in these samples. It is clear that the stellar feedback strength has a strong effect on the absolute metallicity of halos in the sample, but the gradient of the mass metallicity relation is largely unchanged. Figure 2.17 shows the slope of the stellar mass metallicity relation of galaxy satellites in these samples plotted against the central galaxy’s metallicity gradient. It is clear that the simulation’s stellar feedback efficiency has a strong effect on galaxy metallicity gradients, but little to no strong effect on the mass-metallicity gradient of their satellites, only changing their absolute metallicity. By limiting the sample to the

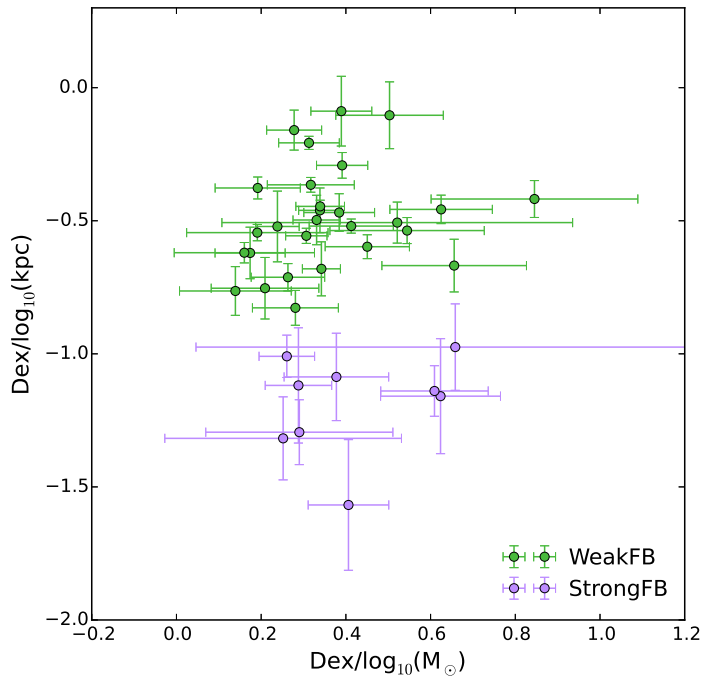


Figure 2.17: Galaxy radial metallicity gradient (y-axis) against the mass-metallicity relation of that galaxy’s $z = 0$ satellites (x-axis). Green points represent the WeakFB model, purple the StrongFB model.

same halos detected in both simulations, it is evident that while the feedback changes the mass-metallicity relation of a galaxy’s satellites, it does not consistently make the gradient stronger or weaker for one run over the other, with some galaxies having a stronger gradient in the stronger feedback model, and an approximately equal number a weaker gradient.

While this is somewhat surprising, it would likely be more informative to investigate correlation with the maximum stellar mass-metallicity relation of the satellites from which a galaxy’s accreted population were deposited,

rather than the $z = 0$ population (e.g. De Lucia and Helmi, 2008).

The simulation with weaker feedback efficiency does, however, predict significantly shallower metallicity gradients compared to the strong feedback model. The likely cause is explained in more detail in S15, who found that the WeakFB (StrongFB) model was able to retain more (less) metal-rich gas owing to the weaker (stronger) outflows, with the effect being most prominent at lower galaxy masses. In Section 2.4 we have shown that one main cause of metallicity gradients is the transition from the in situ dominated to accretion dominated regions. The in situ component of the overall metallicity profile is likely relatively similar in the WeakFB and StrongFB models, however the accreted component (built up primarily from lower mass halos) will be more strongly affected, resulting in an altered overall metallicity profile.

2.7 Outer stellar halo fractions

Recent observational studies have investigated the mass fraction of galaxies contained in their stellar halo (Harmsen et al., 2017). Merritt et al. (2016) measured the stellar halo fraction of 8 spiral galaxies in the Dragonfly Nearby Galaxies Survey, finding a wide variety of outer halo fractions with a mean value of 0.009 ± 0.005 .

To investigate the stellar halo fractions for the galaxies in the EAGLE simulations, we first widen the galaxy selection to include galaxies with stellar masses of $5 \times 10^9 < M_* (M_\odot) < 5 \times 10^{11}$, but keep the disc selection criterion of $D/T > 0.4$. This widens the Ref-L0100N1504 sample to a total of

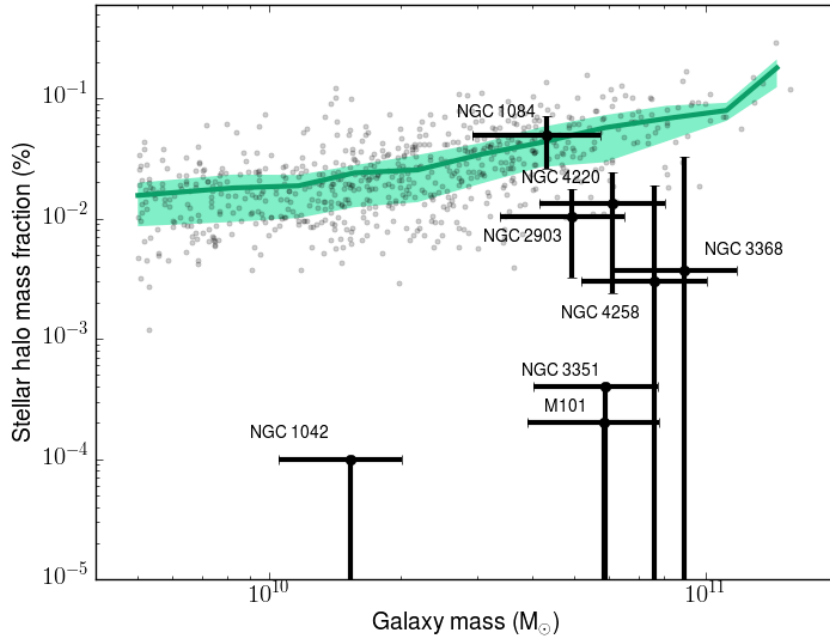


Figure 2.18: Stellar halo mass fraction for a wider range of galaxy masses. The stellar halo is defined as all stars beyond 5 half-light radii. The grey dots are individual galaxies, and green region represents the median and 25th and 75th percentiles. Black dots are observational data from Merritt et al. (2016). Values for NGC 1042, NGC 3351, and M101 are upper limits, with mass fractions consistent with zero.

684 disc galaxies. For the purposes of this analysis we define the stellar halo as stars beyond 5 half-light radii. The half-light radius (R_h) was measured for each galaxy by recording the 2 dimensional radius containing half the galaxy’s total luminosity.

Figure 2.18 shows the stellar halo mass fraction of this expanded sample as a function of their total stellar mass. The sample has an overall mean halo mass fraction of 3%, with the lowest fraction being 0.1% and the highest

30%. The stellar halo mass fraction is correlated with total galaxy stellar mass, rising from a mean fraction of 1% at $M_* \sim 5 \times 10^9 M_\odot$ to 18% at $M_* \sim 5 \times 10^{11} M_\odot$. These values, per our analysis in Section 2.2, are likely to be somewhat higher than the true value as a result of the time resolution.

Also shown on this figure are 8 MW-mass galaxies from the Dragonfly Nearby Galaxies Survey (DNFS, Merritt et al., 2016), whose stellar halo is defined as excess mass from a disk+bulge fit. Only one of these (NGC 1084) is consistent with the EAGLE data set, with two (NGC 2903 and NGC 4220) on the lower edge of the simulated sample. EAGLE fails to reproduce any galaxies with extremely low ($\lesssim 10^{-3}$) outer halo fractions. It is worth noting that the stellar halo definitions used are slightly different. Though both sets of data define the halo beyond 5 half-light radii, DNFS additionally remove mass assigned to the disk and bulge, which could explain the lower fractions observed.

Chapter 3

Conclusions

This study has presented a study of stellar halos in the EAGLE simulation, focusing on the properties of the halos belonging to Milky Way (MW) type galaxies. A number of galaxy samples were analysed, focusing on a set of 9 high resolution galaxies from the Recal-L0025N0752 simulation and 352 lower resolution galaxies from the Ref-L0100N1504 simulation, selecting MW-mass disc galaxies.

EAGLE was found to reproduce a number of observable properties of MW type galaxy stellar halos, including the density and surface brightness profiles. When compared to a range of MW type galaxies, the median surface density profile of EAGLE galaxies broadly covered the observations. The profile had a break at ~ 20 kpc, and power law indices of $\alpha_{inner} = -2.1 \pm 0.5$ and $\alpha_{outer} = -4.0 \pm 0.8$, consistent with those measured for the MW by Deason et al. (2011). The median surface brightness profile was also consistent with recent observations of M31, though more in line with observations along the minor axis of EAGLE galaxies.

Negative metallicity gradients were found to be present across our entire galaxy sample, ranging from -0.002 to -0.02 dex kpc^{-1} . These values are consistent with both recent observations of M31 (Gilbert et al., 2014) and previous hydrodynamical simulations (e.g. Font et al., 2011), but the ubiquity is not consistent with observations (e.g. Monachesi et al., 2016a). By splitting galaxy particles into accreted and in situ components, the negative gradient was found to primarily be driven by the move from high-metallicity stars born in situ to low-metallicity stars accreted through mergers. This does not explain the gradients entirely, as both components also show negative gradients individually, but does appear to be a key piece of information in understanding their cause.

In an effort to understand the origin of flat metallicity profiles observed in some studies, simulation runs with extreme feedback models were also analysed. In these galaxy samples metallicity gradients correlated with feedback strength; stronger feedback led to steeper gradients. This is thought to be a result of the altered feedback efficiency affecting low mass halos primarily. This demonstrates the importance of investigating the sensitivity of results to the chosen subgrid parameters. As observations of stellar halos are often taken along the minor axis, metallicity profiles along major and minor axes were also analysed - no significant differences were found.

The results were tested against simulation runs with mildly varied subgrid physics (primarily AGN and feedback strength). No significant difference in the metallicity or density profiles was found through varying the AGN feedback strength, which is not surprising given their lack of importance at this mass range. The metallicity is affected by up to a few tenths of

a dex, however, with the Reference model having higher metallicity within $\sim 40 - 50$ kpc as compared to models with less realistic feedback dependencies.

The relation between the mass-metallicity relation of a galaxy's satellites and its radial metallicity gradient was investigated, with no correlation found between the $z=0$ mass-metallicity relation and radial metallicity gradient, even when measuring only the gradient of accreted stars. This may not be surprising, however, as the radial metallicity gradient would have theoretically been created by the satellites which already accreted onto the central, and thus investigating correlation with that population may prove more informative. Testing this correlation using two EAGLE models with extremely high and low feedback showed that the mass-metallicity relation is not affected consistently by stellar feedback. While the radial metallicity gradient changes in the presence of extremely strong or weak feedback, the mass-metallicity gradient did not.

The outer stellar halo fraction (defined as mass beyond 5 half-light radii) of galaxies in a wider mass range were measured for comparison with recent stellar halo surveys. The stellar halo mass fraction of EAGLE galaxies was found to be correlated with galaxy stellar mass, with the mean fraction rising from 1% at $M_* \sim 5 \times 10^9 M_\odot$ to 18% at $M_* \sim 5 \times 10^{11} M_\odot$. The sample has an overall mean halo mass fraction of 3%, ranging from 0.1% to 30%. These results were broadly inconsistent with stellar halo fractions measured in the Dragonfly Nearby Galaxies Survey, though a possible confounding factor is the slightly different outer stellar halo definitions used.

Chapter 4

Future Work

The results presented in this study can form the basis of future work investigating the stellar halos of galaxies in the EAGLE simulations. This chapter outlines some potential avenues of study that would continue the work detailed here.

4.1 Metallicity profiles

Disagreement remains between observations of stellar halo metallicity distributions and predictions from simulations. While observations detect negative metallicity gradients in only some galaxies, simulations - including EAGLE - are consistently negative in the Milky Way (MW) mass range. In this work it was shown that the simulation feedback strength plays a strong part in the steepness of galaxy metallicity gradients, with stronger feedback eliciting a steeper gradient. In further study there is scope to investigate the gradient strength dependency further - what other mechanisms and inputs

alter the strength and shape of metallicity gradients in the EAGLE simulations? Does a galaxy's merger history affect the metallicity gradient, for example?

The diversity of metallicity profiles was shown here (Figure 2.11), but not investigated in detail. Future studies could investigate what causes one galaxy to have a metallicity profile that is mostly flat, with a short and steep decline, while another smoothly decreases in metallicity from the inner to outer regions. The origin of the in situ metallicity gradient was also not investigated in detail. The accreted population can likely be explained by the behaviour of accreted satellites, but the in situ population requires a different explanation. Future work could investigate the origin of this gradient, exploring avenues such as kinematic heating during mergers and the migration of stars during their life.

Figure 2.15 showed the mass-metallicity relation of satellites of the galaxies analysed in the rest of this work. It may be more informative, however, to investigate the relation - and its correlation with other properties - of the satellites which were previously accreted into the galaxy. This is likely to uncover more interesting results as it will have directly impacted the $z = 0$ galaxy properties.

4.2 Stellar halo diversity

This work has focused on disc dominated galaxies of approximately MW mass. This is only a narrow window on galaxy populations as a whole, however. Future study could apply the investigations carried out here to

wider mass ranges, exploring the galaxy mass dependence to uncover new insights. Comparisons between galaxies of different types (i.e. early vs. late type), environments, and merger histories would may prove enlightening, and could explain ongoing discrepancies between observations and theory.

It would also be informative to split some of the generalised results into per-galaxy investigations, such as measurements of the density profile break radii of individual galaxies (rather than the median profile) and quantifying the shape of metallicity profiles.

4.3 Stellar halo fractions

Stellar halos are defined in varying ways from one study to the next, especially when comparing observations to theoretical data sets. Future work could be done using the EAGLE simulations to explore these definitions and come to a conclusion on how comparable they are.

By taking a data set from EAGLE (such as the ones analysed here), and applying a range of observational and theoretical stellar halo definitions to the same galaxies, a future study could investigate the stellar halo fractions calculated through each definition. Such a study could conclude which observational techniques are most reliable (since the simulation knows the 'true' answer), as well as making recommendations for how to best compare a theoretical (usually kinematic) definition of the stellar halo, with one based on observational metrics.

Bibliography

- M. G. Abadi, J. F. Navarro, M. Steinmetz, and V. R. Eke. Simulations of Galaxy Formation in a Λ Cold Dark Matter Universe. I. Dynamical and Photometric Properties of a Simulated Disk Galaxy. *ApJ*, 591:499–514, July 2003. doi: 10.1086/375512.
- D. An, T. C. Beers, J. A. Johnson, M. H. Pinsonneault, Y. S. Lee, J. Bovy, Ž. Ivezić, D. Carollo, and M. Newby. The Stellar Metallicity Distribution Function of the Galactic Halo from SDSS Photometry. *ApJ*, 763:65, January 2013. doi: 10.1088/0004-637X/763/1/65.
- J. Bailin, E. F. Bell, M. Valluri, G. S. Stinson, V. P. Debattista, H. M. P. Couchman, and J. Wadsley. Systematic Problems with Using Dark Matter Simulations to Model Stellar Halos. *ApJ*, 783:95, March 2014. doi: 10.1088/0004-637X/783/2/95.
- J. Bakos and I. Trujillo. Deep Surface Brightness Profiles of Spiral Galaxies from SDSS Stripe82: Touching Stellar Halos. *ArXiv e-prints*, April 2012.
- M. K. Barker, A. M. N. Ferguson, M. Irwin, N. Arimoto, and P. Jablonka. Resolving the Stellar Outskirts of M81: Evidence for a Faint, Extended Structural Component. *AJ*, 138:1469–1484, November 2009. doi: 10.1088/0004-6256/138/5/1469.
- M. K. Barker, A. M. N. Ferguson, M. J. Irwin, N. Arimoto, and P. Jablonka. Quantifying the faint structure of galaxies: the late-type spiral NGC 2403. *MNRAS*, 419:1489–1506, January 2012. doi: 10.1111/j.1365-2966.2011.19814.x.
- P. Barmby, M. L. N. Ashby, L. Bianchi, C. W. Engelbracht, R. D. Gehrz, K. D. Gordon, J. L. Hinz, J. P. Huchra, R. M. Humphreys, M. A. Pahre, P. G. Pérez-González, E. F. Polomski, G. H. Rieke, D. A. Thilker, S. P. Willner, and C. E. Woodward. Dusty Waves on a Starry Sea: The Mid-Infrared View of M31. *ApJ*, 650:L45–L49, October 2006. doi: 10.1086/508626.
- P. Barmby, M. L. N. Ashby, L. Bianchi, C. W. Engelbracht, R. D. Gehrz, K. D. Gordon, J. L. Hinz, J. P. Huchra, R. M. Humphreys, M. A. Pahre, P. G. Pérez-González, E. F. Polomski, G. H. Rieke, D. A. Thilker, S. P. Willner, and C. E. Woodward. Erratum: “Dusty Waves on a Starry Sea: The Mid-Infrared View of M31” ([jA href="/abs/2006ApJ..650L..45"](/abs/2006ApJ..650L..45)) *ApJ* 650, L45 [2006]i/A*l*). *ApJ*, 655:L61–L61, January 2007. doi: 10.1086/511682.
- T. C. Beers, D. Carollo, Ž. Ivezić, D. An, M. Chiba, J. E. Norris, K. C. Freeman, Y. S. Lee, J. A. Munn, P. Re Fiorentin, T. Sivarani, R. Wilhelm, B. Yanny, and D. G. York.

- The Case for the Dual Halo of the Milky Way. *ApJ*, 746:34, February 2012. doi: 10.1088/0004-637X/746/1/34.
- E. F. Bell, D. B. Zucker, V. Belokurov, S. Sharma, K. V. Johnston, J. S. Bullock, D. W. Hogg, K. Jahnke, J. T. A. de Jong, T. C. Beers, N. W. Evans, E. K. Grebel, Ž. Ivezić, S. E. Koposov, H.-W. Rix, D. P. Schneider, M. Steinmetz, and A. Zolotov. The Accretion Origin of the Milky Way’s Stellar Halo. *ApJ*, 680:295-311, June 2008. doi: 10.1086/588032.
- V. Belokurov, D. B. Zucker, N. W. Evans, G. Gilmore, S. Vidrih, D. M. Bramich, H. J. Newberg, R. F. G. Wyse, M. J. Irwin, M. Fellhauer, P. C. Hewett, N. A. Walton, M. I. Wilkinson, N. Cole, B. Yanny, C. M. Rockosi, T. C. Beers, E. F. Bell, J. Brinkmann, Ž. Ivezić, and R. Lupton. The Field of Streams: Sagittarius and Its Siblings. *ApJ*, 642:L137–L140, May 2006. doi: 10.1086/504797.
- J. Bland-Hawthorn and O. Gerhard. The Galaxy in Context: Structural, Kinematic, and Integrated Properties. *ARA&A*, 54:529–596, September 2016. doi: 10.1146/annurev-astro-081915-023441.
- H. Bondi and F. Hoyle. On the mechanism of accretion by stars. *MNRAS*, 104:273, 1944. doi: 10.1093/mnras/104.5.273.
- M. Boylan-Kolchin, J. S. Bullock, S. T. Sohn, G. Besla, and R. P. van der Marel. The Space Motion of Leo I: The Mass of the Milky Way’s Dark Matter Halo. *ApJ*, 768:140, May 2013. doi: 10.1088/0004-637X/768/2/140.
- J. S. Bullock and K. V. Johnston. Tracing Galaxy Formation with Stellar Halos. I. Methods. *ApJ*, 635:931–949, December 2005. doi: 10.1086/497422.
- D. Carollo, T. C. Beers, Y. S. Lee, M. Chiba, J. E. Norris, R. Wilhelm, T. Sivarani, B. Marsteller, J. A. Munn, C. A. L. Bailer-Jones, P. R. Fiorentin, and D. G. York. Two stellar components in the halo of the Milky Way. *Nature*, 450:1020–1025, December 2007. doi: 10.1038/nature06460.
- G. Clementini. RR Lyrae Stars in Dwarf Spheroidal Galaxies. In C. Sterken, N. Samus, and L. Szabados, editors, *Variable Stars, the Galactic halo and Galaxy Formation*, February 2010.
- A. P. Cooper, S. Cole, C. S. Frenk, S. D. M. White, J. Helly, A. J. Benson, G. De Lucia, A. Helmi, A. Jenkins, J. F. Navarro, V. Springel, and J. Wang. Galactic stellar haloes in the CDM model. *MNRAS*, 406:744–766, August 2010. doi: 10.1111/j.1365-2966.2010.16740.x.
- A. P. Cooper, O. H. Parry, B. Lowing, S. Cole, and C. Frenk. Formation of in situ stellar haloes in Milky Way-mass galaxies. *MNRAS*, 454:3185–3199, December 2015. doi: 10.1093/mnras/stv2057.
- R. A. Crain, T. Theuns, C. Dalla Vecchia, V. R. Eke, C. S. Frenk, A. Jenkins, S. T. Kay, J. A. Peacock, F. R. Pearce, J. Schaye, V. Springel, P. A. Thomas, S. D. M. White, and R. P. C. Wiersma. Galaxies-intergalactic medium interaction calculation - I. Galaxy formation as a function of large-scale environment. *MNRAS*, 399:1773–1794, November 2009. doi: 10.1111/j.1365-2966.2009.15402.x.

- M. Davis, G. Efstathiou, C. S. Frenk, and S. D. M. White. The evolution of large-scale structure in a universe dominated by cold dark matter. *ApJ*, 292:371–394, May 1985. doi: 10.1086/163168.
- J. T. A. de Jong, B. Yanny, H.-W. Rix, A. E. Dolphin, N. F. Martin, and T. C. Beers. Mapping the Stellar Structure of the Milky Way Thick Disk and Halo Using SEGUE Photometry. *ApJ*, 714:663–674, May 2010. doi: 10.1088/0004-637X/714/1/663.
- G. De Lucia and A. Helmi. The Galaxy and its stellar halo: insights on their formation from a hybrid cosmological approach. *MNRAS*, 391:14–31, November 2008. doi: 10.1111/j.1365-2966.2008.13862.x.
- A. J. Deason, V. Belokurov, and N. W. Evans. The Milky Way stellar halo out to 40 kpc: squashed, broken but smooth. *MNRAS*, 416:2903–2915, October 2011. doi: 10.1111/j.1365-2966.2011.19237.x.
- A. J. Deason, V. Belokurov, N. W. Evans, and K. V. Johnston. Broken and Unbroken: The Milky Way and M31 Stellar Halos. *ApJ*, 763:113, February 2013. doi: 10.1088/0004-637X/763/2/113.
- A. J. Deason, V. Belokurov, S. E. Koposov, and C. M. Rockosi. Touching The Void: A Striking Drop in Stellar Halo Density Beyond 50 kpc. *ApJ*, 787:30, May 2014. doi: 10.1088/0004-637X/787/1/30.
- A. J. Deason, V. Belokurov, and D. R. Weisz. The progenitors of the Milky Way stellar halo: big bricks favoured over little bricks. *MNRAS*, 448:L77–L81, March 2015. doi: 10.1093/mnras/slv001.
- A. J. Deason, V. Belokurov, S. E. Koposov, F. A. Gomez, R. J. Grand, F. Marinacci, and R. Pakmor. The slight spin of the old stellar halo. *ArXiv e-prints*, March 2017.
- K. Dolag, S. Borgani, G. Murante, and V. Springel. Substructures in hydrodynamical cluster simulations. *MNRAS*, 399:497–514, October 2009. doi: 10.1111/j.1365-2966.2009.15034.x.
- R. D’Souza, G. Kauffman, J. Wang, and S. Vegetti. Parametrizing the stellar haloes of galaxies. *MNRAS*, 443:1433–1450, September 2014. doi: 10.1093/mnras/stu1194.
- M. A. Fardal, M. D. Weinberg, A. Babul, M. J. Irwin, P. Guhathakurta, K. M. Gilbert, A. M. N. Ferguson, R. A. Ibata, G. F. Lewis, N. R. Tanvir, and A. P. Huxor. Inferring the Andromeda Galaxy’s mass from its giant southern stream with Bayesian simulation sampling. *MNRAS*, 434:2779–2802, October 2013. doi: 10.1093/mnras/stt1121.
- A. Fattahi, J. F. Navarro, T. Sawala, C. S. Frenk, K. A. Oman, R. A. Crain, M. Furlong, M. Schaller, J. Schaye, T. Theuns, and A. Jenkins. The APOSTLE project: Local Group kinematic mass constraints and simulation candidate selection. *MNRAS*, 457: 844–856, March 2016. doi: 10.1093/mnras/stv2970.
- A. S. Font, K. V. Johnston, J. S. Bullock, and B. E. Robertson. Chemical Abundance Distributions of Galactic Halos and Their Satellite Systems in a Λ CDM Universe. *ApJ*, 638:585–595, February 2006. doi: 10.1086/498970.

- A. S. Font, K. V. Johnston, A. M. N. Ferguson, J. S. Bullock, B. E. Robertson, J. Tumlinson, and P. Guhathakurta. The Stellar Content of Galaxy Halos: A Comparison between Λ CDM Models and Observations of M31. *ApJ*, 673:215–225, January 2008. doi: 10.1086/524102.
- A. S. Font, I. G. McCarthy, R. A. Crain, T. Theuns, J. Schaye, R. P. C. Wiersma, and C. Dalla Vecchia. Cosmological simulations of the formation of the stellar haloes around disc galaxies. *MNRAS*, 416:2802–2820, October 2011. doi: 10.1111/j.1365-2966.2011.19227.x.
- A. Frebel, E. N. Kirby, and J. D. Simon. Linking dwarf galaxies to halo building blocks with the most metal-poor star in Sculptor. *Nature*, 464:72–75, March 2010. doi: 10.1038/nature08772.
- K. Freeman and J. Bland-Hawthorn. The New Galaxy: Signatures of Its Formation. *ARA&A*, 40:487–537, 2002. doi: 10.1146/annurev.astro.40.060401.093840.
- M. Furlong, R. G. Bower, T. Theuns, J. Schaye, R. A. Crain, M. Schaller, C. Dalla Vecchia, C. S. Frenk, I. G. McCarthy, J. Helly, A. Jenkins, and Y. M. Rosas-Guevara. Evolution of galaxy stellar masses and star formation rates in the EAGLE simulations. *MNRAS*, 450:4486–4504, July 2015. doi: 10.1093/mnras/stv852.
- M. Furlong, R. G. Bower, R. A. Crain, J. Schaye, T. Theuns, J. W. Trayford, Y. Qu, M. Schaller, M. Berthet, and J. C. Helly. Size evolution of normal and compact galaxies in the EAGLE simulation. *MNRAS*, 465:722–738, February 2017. doi: 10.1093/mnras/stw2740.
- A. Gallazzi, S. Charlot, J. Brinchmann, S. D. M. White, and C. A. Tremonti. The ages and metallicities of galaxies in the local universe. *MNRAS*, 362:41–58, September 2005. doi: 10.1111/j.1365-2966.2005.09321.x.
- K. M. Gilbert, P. Guhathakurta, R. L. Beaton, J. Bullock, M. C. Geha, J. S. Kalirai, E. N. Kirby, S. R. Majewski, J. C. Ostheimer, R. J. Patterson, E. J. Tollerud, M. Tanaka, and M. Chiba. Global Properties of M31’s Stellar Halo from the SPLASH Survey. I. Surface Brightness Profile. *ApJ*, 760:76, November 2012. doi: 10.1088/0004-637X/760/1/76.
- K. M. Gilbert, J. S. Kalirai, P. Guhathakurta, R. L. Beaton, M. C. Geha, E. N. Kirby, S. R. Majewski, R. J. Patterson, E. J. Tollerud, J. S. Bullock, M. Tanaka, and M. Chiba. Global Properties of M31’s Stellar Halo from the SPLASH Survey. II. Metallicity Profile. *ApJ*, 796:76, December 2014. doi: 10.1088/0004-637X/796/2/76.
- A. Gould. An Upper Limit on the Granularity of the Local Stellar Halo. *ApJ*, 592:L63–L66, August 2003. doi: 10.1086/377525.
- Carl J. Grillmair and Jeffrey L. Carlin. *Stellar Streams and Clouds in the Galactic Halo*, pages 87–112. Springer International Publishing, Cham, 2016. ISBN 978-3-319-19336-6. doi: 10.1007/978-3-319-19336-6.
- Q. Guo, S. White, C. Li, and M. Boylan-Kolchin. How do galaxies populate dark matter haloes? *MNRAS*, 404:1111–1120, May 2010. doi: 10.1111/j.1365-2966.2010.16341.x.

- J. A. Guzik, L. S. Watson, and A. N. Cox. Can Enhanced Diffusion Improve Helioseismic Agreement for Solar Models with Revised Abundances? *ApJ*, 627:1049–1056, July 2005. doi: 10.1086/430438.
- B. Harmsen, A. Monachesi, E. F. Bell, R. S. de Jong, J. Bailin, D. J. Radburn-Smith, and B. W. Holwerda. Diverse stellar haloes in nearby Milky Way mass disc galaxies. *MNRAS*, 466:1491–1512, April 2017. doi: 10.1093/mnras/stw2992.
- A. Helmi. The stellar halo of the Galaxy. *A&A Rev.*, 15:145–188, June 2008. doi: 10.1007/s00159-008-0009-6.
- A. Helmi, S. D. M. White, P. T. de Zeeuw, and H. Zhao. Debris streams in the solar neighbourhood as relicts from the formation of the Milky Way. *Nature*, 402:53–55, November 1999. doi: 10.1038/46980.
- A. Helmi, J. Veljanoski, M. A. Breddels, H. Tian, and L. V. Sales. A box full of chocolates: The rich structure of the nearby stellar halo revealed by Gaia and RAVE. *A&A*, 598:A58, January 2017. doi: 10.1051/0004-6361/201629990.
- R. Ibata, S. Chapman, A. M. N. Ferguson, M. Irwin, G. Lewis, and A. McConnachie. Taking measure of the Andromeda halo: a kinematic analysis of the giant stream surrounding M31. *MNRAS*, 351:117–124, June 2004. doi: 10.1111/j.1365-2966.2004.07759.x.
- R. A. Ibata, G. F. Lewis, A. W. McConnachie, N. F. Martin, M. J. Irwin, A. M. N. Ferguson, A. Babul, E. J. Bernard, S. C. Chapman, M. Collins, M. Fardal, A. D. Mackey, J. Navarro, J. Peñarrubia, R. M. Rich, N. Tanvir, and L. Widrow. The Large-scale Structure of the Halo of the Andromeda Galaxy. I. Global Stellar Density, Morphology and Metallicity Properties. *ApJ*, 780:128, January 2014. doi: 10.1088/0004-637X/780/2/128.
- Ž. Ivezić, B. Sesar, M. Jurić, N. Bond, J. Dalcanton, C. M. Rockosi, B. Yanny, H. J. Newberg, T. C. Beers, C. Allende Prieto, R. Wilhelm, Y. S. Lee, T. Sivarani, J. E. Norris, C. A. L. Bailer-Jones, P. Re Fiorentin, D. Schlegel, A. Uomoto, R. H. Lupton, G. R. Knapp, J. E. Gunn, K. R. Covey, J. Allyn Smith, G. Miknaitis, M. Doi, M. Tanaka, M. Fukugita, S. Kent, D. Finkbeiner, J. A. Munn, J. R. Pier, T. Quinn, S. Hawley, S. Anderson, F. Kiuchi, A. Chen, J. Bushong, H. Sohi, D. Haggard, A. Kimball, J. Barentine, H. Brewington, M. Harvanek, S. Kleinman, J. Krzesinski, D. Long, A. Nitta, S. Snedden, B. Lee, H. Harris, J. Brinkmann, D. P. Schneider, and D. G. York. The Milky Way Tomography with SDSS. II. Stellar Metallicity. *ApJ*, 684:287–325, September 2008. doi: 10.1086/589678.
- Ž. Ivezić, T. C. Beers, and M. Jurić. Galactic Stellar Populations in the Era of the Sloan Digital Sky Survey and Other Large Surveys. *ARA&A*, 50:251–304, September 2012. doi: 10.1146/annurev-astro-081811-125504.
- M. Jurić, Ž. Ivezić, A. Brooks, R. H. Lupton, D. Schlegel, D. Finkbeiner, N. Padmanabhan, N. Bond, B. Sesar, C. M. Rockosi, G. R. Knapp, J. E. Gunn, T. Sumi, D. P. Schneider, J. C. Barentine, H. J. Brewington, J. Brinkmann, M. Fukugita, M. Harvanek, S. J. Kleinman, J. Krzesinski, D. Long, E. H. Nielsen, Jr., A. Nitta, S. A. Snedden, and D. G. York. The Milky Way Tomography with SDSS. I. Stellar Number Density Distribution. *ApJ*, 673:864–914, February 2008. doi: 10.1086/523619.

- P. R. Kafle, S. Sharma, G. F. Lewis, and J. Bland-Hawthorn. On the Shoulders of Giants: Properties of the Stellar Halo and the Milky Way Mass Distribution. *ApJ*, 794:59, October 2014. doi: 10.1088/0004-637X/794/1/59.
- I. D. Karachentsev and O. G. Kashibadze. Masses of the local group and of the M81 group estimated from distortions in the local velocity field. *Astrophysics*, 49:3–18, January 2006. doi: 10.1007/s10511-006-0002-6.
- A. A. Képley, H. L. Morrison, A. Helmi, T. D. Kinman, J. Van Duyne, J. C. Martin, P. Harding, J. E. Norris, and K. C. Freeman. Halo Star Streams in the Solar Neighborhood. *AJ*, 134:1579–1595, October 2007. doi: 10.1086/521429.
- E. N. Kirby, J. G. Cohen, P. Guhathakurta, L. Cheng, J. S. Bullock, and A. Gallazzi. The Universal Stellar Mass–Stellar Metallicity Relation for Dwarf Galaxies. *ApJ*, 779:102, December 2013. doi: 10.1088/0004-637X/779/2/102.
- R. Klement, H.-W. Rix, C. Flynn, B. Fuchs, T. C. Beers, C. Allende Prieto, D. Bizyaev, H. Brewington, Y. S. Lee, E. Malanushenko, V. Malanushenko, D. Oravetz, K. Pan, P. Re Fiorentin, A. Simmons, and S. Snedden. Halo Streams in the Seventh Sloan Digital Sky Survey Data Release. *ApJ*, 698:865–894, June 2009. doi: 10.1088/0004-637X/698/1/865.
- C. d. P. Lagos, T. Theuns, J. Schaye, M. Furlong, R. G. Bower, M. Schaller, R. A. Crain, J. W. Trayford, and J. Matthee. The Fundamental Plane of star formation in galaxies revealed by the EAGLE hydrodynamical simulations. *MNRAS*, 459:2632–2650, July 2016. doi: 10.1093/mnras/stw717.
- N. I. Libeskind, A. Knebe, Y. Hoffman, S. Gottlöber, and G. Yepes. Disentangling the dark matter halo from the stellar halo. *MNRAS*, 418:336–345, November 2011. doi: 10.1111/j.1365-2966.2011.19487.x.
- T. C. Licquia and J. A. Newman. Improved Estimates of the Milky Way’s Stellar Mass and Star Formation Rate from Hierarchical Bayesian Meta-Analysis. *ApJ*, 806:96, June 2015. doi: 10.1088/0004-637X/806/1/96.
- I. G. McCarthy, A. S. Font, R. A. Crain, A. J. Deason, J. Schaye, and T. Theuns. Global structure and kinematics of stellar haloes in cosmological hydrodynamic simulations. *MNRAS*, 420:2245–2262, March 2012. doi: 10.1111/j.1365-2966.2011.20189.x.
- P. J. McMillan. Mass models of the Milky Way. *MNRAS*, 414:2446–2457, July 2011. doi: 10.1111/j.1365-2966.2011.18564.x.
- P. J. McMillan. The mass distribution and gravitational potential of the Milky Way. *MNRAS*, 465:76–94, February 2017. doi: 10.1093/mnras/stw2759.
- A. Merritt, P. van Dokkum, R. Abraham, and J. Zhang. The Dragonfly nearby Galaxies Survey. I. Substantial Variation in the Diffuse Stellar Halos around Spiral Galaxies. *ApJ*, 830:62, October 2016. doi: 10.3847/0004-637X/830/2/62.
- A. Monachesi, E. F. Bell, D. J. Radburn-Smith, J. Bailin, R. S. de Jong, B. Holwerda, D. Streich, and G. Silverstein. The GHOSTS survey - II. The diversity of halo colour and metallicity profiles of massive disc galaxies. *MNRAS*, 457:1419–1446, April 2016a. doi: 10.1093/mnras/stv2987.

- A. Monachesi, F. A. Gómez, R. J. J. Grand, G. Kauffmann, F. Marinacci, R. Pakmor, V. Springel, and C. S. Frenk. On the stellar halo metallicity profile of Milky Way-like galaxies in the Auriga simulations. *MNRAS*, 459:L46–L50, June 2016b. doi: 10.1093/mnrasl/slw052.
- H. L. Morrison, M. Mateo, E. W. Olszewski, P. Harding, R. C. Dohm-Palmer, K. C. Freeman, J. E. Norris, and M. Morita. Mapping the Galactic Halo. I. The “Spaghetti” Survey. *AJ*, 119:2254–2273, May 2000. doi: 10.1086/301357.
- H. J. Newberg and B. Yanny. The Milky Way’s stellar halo - lumpy or triaxial? In *Journal of Physics Conference Series*, volume 47 of *Journal of Physics Conference Series*, pages 195–204, October 2006. doi: 10.1088/1742-6596/47/1/024.
- H. J. Newberg, B. Yanny, C. Rockosi, E. K. Grebel, H.-W. Rix, J. Brinkmann, I. Csabai, G. Hennessy, R. B. Hindsley, R. Ibata, Z. Ivezić, D. Lamb, E. T. Nash, M. Odenkirchen, H. A. Rave, D. P. Schneider, J. A. Smith, A. Stolte, and D. G. York. The Ghost of Sagittarius and Lumps in the Halo of the Milky Way. *ApJ*, 569:245–274, April 2002. doi: 10.1086/338983.
- J. Peñarrubia, F. A. Gómez, G. Besla, D. Erkal, and Y.-Z. Ma. A timing constraint on the (total) mass of the Large Magellanic Cloud. *MNRAS*, 456:L54–L58, February 2016. doi: 10.1093/mnrasl/slv160.
- A. Pillepich, P. Madau, and L. Mayer. Building Late-type Spiral Galaxies by In-situ and Ex-situ Star Formation. *ApJ*, 799:184, February 2015. doi: 10.1088/0004-637X/799/2/184.
- Planck Collaboration I. Planck 2013 results. I. Overview of products and scientific results. *A&A*, 571:A1, November 2014. doi: 10.1051/0004-6361/201321529.
- Planck Collaboration XVI. Planck 2013 results. XVI. Cosmological parameters. *A&A*, 571:A16, November 2014. doi: 10.1051/0004-6361/201321591.
- D. J. Radburn-Smith, R. S. de Jong, A. C. Seth, J. Bailin, E. F. Bell, T. M. Brown, J. S. Bullock, S. Courteau, J. J. Dalcanton, H. C. Ferguson, P. Goudfrooij, S. Holfeltz, B. W. Holwerda, C. Purcell, J. Sick, D. Streich, M. Vlahic, and D. B. Zucker. The GHOSTS Survey. I. Hubble Space Telescope Advanced Camera for Surveys Data. *ApJS*, 195:18, August 2011. doi: 10.1088/0067-0049/195/2/18.
- V. Rashkov, A. Pillepich, A. J. Deason, P. Madau, C. M. Rockosi, J. Guedes, and L. Mayer. A “Light,” Centrally Concentrated Milky Way Halo? *ApJ*, 773:L32, August 2013. doi: 10.1088/2041-8205/773/2/L32.
- A. C. Robin, C. Reylé, and M. Crézé. Early galaxy evolution from deep wide field star counts. I. The spheroid density law and mass function. *A&A*, 359:103–112, July 2000.
- S. Ruphy, A. C. Robin, N. Epchtein, E. Copet, E. Bertin, P. Fouque, and F. Guglielmo. New determination of the disc scale length and the radial cutoff in the anticenter with DENIS data. *A&A*, 313:L21–L24, September 1996.

- L. V. Sales, J. F. Navarro, J. Schaye, C. Dalla Vecchia, V. Springel, and C. M. Booth. Feedback and the structure of simulated galaxies at redshift $z=2$. *MNRAS*, 409:1541–1556, December 2010. doi: 10.1111/j.1365-2966.2010.17391.x.
- J. Schaye, R. A. Crain, R. G. Bower, M. Furlong, M. Schaller, T. Theuns, C. Dalla Vecchia, C. S. Frenk, I. G. McCarthy, J. C. Helly, A. Jenkins, Y. M. Rosas-Guevara, S. D. M. White, M. Baes, C. M. Booth, P. Camps, J. F. Navarro, Y. Qu, A. Rahmati, T. Sawala, P. A. Thomas, and J. Trayford. The EAGLE project: simulating the evolution and assembly of galaxies and their environments. *MNRAS*, 446:521–554, January 2015. doi: 10.1093/mnras/stu2058.
- R. Schönrich, M. Asplund, and L. Casagrande. On the alleged duality of the Galactic halo. *MNRAS*, 415:3807–3823, August 2011. doi: 10.1111/j.1365-2966.2011.19003.x.
- R. Schönrich, M. Asplund, and L. Casagrande. Does SEGUE/SDSS indicate a dual Galactic halo? *ApJ*, 786:7, May 2014. doi: 10.1088/0004-637X/786/1/7.
- B. Sesar, M. Jurić, and Ž. Ivezić. The Shape and Profile of the Milky Way Halo as Seen by the Canada-France-Hawaii Telescope Legacy Survey. *ApJ*, 731:4, April 2011. doi: 10.1088/0004-637X/731/1/4.
- M. H. Siegel, S. R. Majewski, I. N. Reid, and I. B. Thompson. Star Counts Redivivus. IV. Density Laws through Photometric Parallaxes. *ApJ*, 578:151–175, October 2002. doi: 10.1086/342469.
- V. Springel. The cosmological simulation code GADGET-2. *MNRAS*, 364:1105–1134, December 2005. doi: 10.1111/j.1365-2966.2005.09655.x.
- V. Springel, S. D. M. White, G. Tormen, and G. Kauffmann. Populating a cluster of galaxies - I. Results at $z=0$. *MNRAS*, 328:726–750, December 2001. doi: 10.1046/j.1365-8711.2001.04912.x.
- G. S. Stinson, J. Bailin, H. Couchman, J. Wadsley, S. Shen, S. Nickerson, C. Brook, and T. Quinn. Cosmological galaxy formation simulations using smoothed particle hydrodynamics. *MNRAS*, 408:812–826, October 2010. doi: 10.1111/j.1365-2966.2010.17187.x.
- T. Tal and P. G. van Dokkum. The Faint Stellar Halos of Massive Red Galaxies from Stacks of More than 42,000 SDSS LRG Images. *ApJ*, 731:89, April 2011. doi: 10.1088/0004-637X/731/2/89.
- A. Tamm, E. Tempel, P. Tenjes, O. Tihhonova, and T. Tuvikene. Stellar mass map and dark matter distribution in M 31. *A&A*, 546:A4, October 2012. doi: 10.1051/0004-6361/201220065.
- M. Tanaka, M. Chiba, Y. Komiyama, P. Guhathakurta, J. S. Kalirai, and M. Iye. Structure and Population of the Andromeda Stellar Halo from a Subaru/Suprime-Cam Survey. *ApJ*, 708:1168–1203, January 2010. doi: 10.1088/0004-637X/708/2/1168.
- P. B. Tissera, C. Scannapieco, T. C. Beers, and D. Carollo. Stellar haloes of simulated Milky-Way-like galaxies: chemical and kinematic properties. *MNRAS*, 432:3391–3400, July 2013. doi: 10.1093/mnras/stt691.

- P. B. Tissera, T. C. Beers, D. Carollo, and C. Scannapieco. Stellar haloes in Milky Way mass galaxies: from the inner to the outer haloes. *MNRAS*, 439:3128–3138, April 2014. doi: 10.1093/mnras/stu181.
- E. J. Tollerud, R. L. Beaton, M. C. Geha, J. S. Bullock, P. Guhathakurta, J. S. Kalirai, S. R. Majewski, E. N. Kirby, K. M. Gilbert, B. Yniguez, R. J. Patterson, J. C. Osheimer, J. Cooke, C. E. Dorman, A. Choudhury, and M. C. Cooper. The SPLASH Survey: Spectroscopy of 15 M31 Dwarf Spheroidal Satellite Galaxies. *ApJ*, 752:45, June 2012. doi: 10.1088/0004-637X/752/1/45.
- J. W. Trayford, T. Theuns, R. G. Bower, J. Schaye, M. Furlong, M. Schaller, C. S. Frenk, R. A. Crain, C. Dalla Vecchia, and I. G. McCarthy. Colours and luminosities of $z = 0.1$ galaxies in the EAGLE simulation. *MNRAS*, 452:2879–2896, September 2015. doi: 10.1093/mnras/stv1461.
- J. W. Trayford, T. Theuns, R. G. Bower, R. A. Crain, C. d. P. Lagos, M. Schaller, and J. Schaye. It is not easy being green: the evolution of galaxy colour in the EAGLE simulation. *MNRAS*, 460:3925–3939, August 2016. doi: 10.1093/mnras/stw1230.
- I. Trujillo and J. Bakos. Stellar haloes of disc galaxies at $z \sim 1$. *MNRAS*, 431:1121–1135, May 2013. doi: 10.1093/mnras/stt232.
- R. A. M. Walterbos and R. C. Kennicutt, Jr. An optical study of stars and dust in the Andromeda galaxy. *A&A*, 198:61–86, June 1988.
- X.-X. Xue, H.-W. Rix, Z. Ma, H. Morrison, J. Bovy, B. Sesar, and W. Janesh. The Radial Profile and Flattening of the Milky Way’s Stellar Halo to 80 kpc from the SEGUE K-giant Survey. *ApJ*, 809:144, August 2015. doi: 10.1088/0004-637X/809/2/144.